Contributions to Mineralogy and Petrology (2018) 173:61
https://doi.org/10.1007/s00410-018-1486-x

ORIGINAL PAPER

Combining textural and geochemical investigations to explore the dynamics of magma ascent during Plinian eruptions: a Somma–Vesuvius volcano (Italy) case study

L. Pappalardo[1] · G. Buono[1,2] · S. Fanara[3] · P. Petrosino[2]

Received: 20 February 2018 / Accepted: 20 June 2018 / Published online: 9 July 2018

Abstract
Trigger mechanisms and syn-eruptive processes of Plinian eruptions are poorly understood especially in the case of mafic powerful events. In the last decades, the combined geochemical and textural studies on volcanic rocks have proven to be fundamental tools for exploring the dynamics of magma ascent in volcanic conduits and for improving our ability to interpret volcano-monitoring signals and assess hazard. In this case study, we quantitatively investigate 2D and 3D micro-textural, geochemical, and isotopic features of pyroclastic rocks erupted during the Pomici di Base Plinian eruption (22 ka), the generally acknowledged first and most powerful event of the Somma–Vesuvius volcano. A peculiar aspect of this eruption is its high intensity that remained stable during the entire Plinian phase despite the strong magma compositional variation towards mafic terms. We infer that the transfer of magma towards the surface was intensified by the occurrence of rapid vesiculation pulses driven by limestone assimilation (skarn recycling) during magma ascent through the carbonatic bedrock. We conclude that limestone assimilation can hence be a syn-eruptive process, able to trigger further gas nucleation with deep impact on the eruption intensity, particularly crucial in the case of mafic/intermediate magma compositions.

Keywords Plinian eruptions · Syn-eruptive processes · Limestone assimilation · X-ray computed microtomography

Introduction

In the twentieth century, at least a dozen of worldwide strato-volcanoes generated high-magnitude eruptions that killed thousands of people and caused extensive damage with severe social and economic impacts. Some of these events interrupted long lasting periods of quiescence (e.g., Pinatubo, Philippines, 1991), while others followed a short volcanic rest (e.g., Colima, Mexico, 1913) or occurred with only little warning (e.g., Chaiten, Chile, 2008). Hence, understanding the trigger mechanisms as well as the syn-eruptive dynamics of these eruptions is crucial for their forecasting. Combined quantitative textural and geochemical studies on volcanic rocks have proven to be a valuable approach in exploring the conditions related to magma ascent in volcanic conduits (e.g., Klug et al. 2002; Adams et al. 2006; Mastrolorenzo and Pappalardo 2006; Gurioli et al. 2008; Polacci et al. 2009, 2014; Shea et al. 2010a, b; Rust and Cashman 2011; Gonnermann and Houghton 2012; Pappalardo et al. 2014; Rotella et al. 2014), improving our ability to interpret volcano-monitoring signals and perform hazard evaluations. Particularly, 3D textural data have played

Communicated by Othmar Müntener.

Electronic supplementary material The online version of this article (https://doi.org/10.1007/s00410-018-1486-x) contains supplementary material, which is available to authorized users.

✉ L. Pappalardo
lucia.pappalardo@ingv.it

[1] Istituto Nazionale di Geofisica e Vulcanologia, Sezione di Napoli-Osservatorio Vesuviano, Via Diocleziano, 328, 80124 Napoli, Italy

[2] DiSTAR-Dipartimento di Scienze della Terra, dell'Ambiente e delle Risorse-Università degli Studi di Napoli Federico II, Complesso Universitario di Monte Sant'Angelo via Cintia, 80126 Napoli, Italy

[3] Institut für Experimentelle und Angewandete Mineralogie, Georg-August Universität Göttingen, Goldschmidt str.1, 37077 Göttingen, Germany

a key role in assessing nucleation, growth, and coalescence of gas bubbles and magma fragmentation that in turn influence the style and intensity of explosive eruptions. In fact, 3D data allow the direct observation and quantification of the dimension, shape, and orientation of the vesicles, as well as of their degree of interconnectedness and related permeability, difficult to determine using the more conventional 2D techniques (e.g., Song et al. 2001; Okumura et al. 2008, 2012; Polacci et al. 2009, 2012, 2014; Degruyter et al. 2010; Giachetti et al. 2011; Baker et al. 2012). X-ray computed microtomography (micro-CT) is a powerful, non-destructive method to carry out 3D textural studies of igneous rocks (e.g., Jerram and Higgins 2007; Baker et al. 2012; Cnudde and Boone 2013). Nevertheless, only a few studies of volcanic pyroclasts using this tool are available especially on alkaline rocks (e.g., Polacci et al. 2009; Hughes et al. 2017).

The Somma–Vesuvius alkaline volcanic complex, located east of the metropolitan area of Naples, is one of the most dangerous volcanoes in the world (e.g., Mastrolorenzo et al. 2008; Lirer et al. 2010; Mastrolorenzo and Pappalardo 2010 and the references therein), Fig. 1. The volcanic activity has been characterized by at least four Plinian eruptions, interposed to minor events covering a large range of magnitude and intensity (Cioni et al. 2008; Santacroce et al. 2008; De Vivo et al. 2010), the latest occurred on March 1944 (e.g., Cole and Scarpati 2010; Pappalardo et al. 2014; Cubellis et al. 2016). The Pomici di Base eruption (Andronico et al. 1995; Delibrias et al. 1979; Bertagnini et al. 1998; Landi et al. 1999; Siani et al. 2004; Santacroce et al. 2008; Klebesz et al. 2012, 2015; Scarpati et al. 2016), occurred about 22 ka, is generally acknowledged as the first and most intense Vesuvian Plinian event. It marks the transition, after a period of prevalent effusive activity, to the explosive behaviour of the volcano as well as the beginning of the caldera collapse events. The eruption was characterized by the emission, during a sustained-column Plinian phase, of at least 4.4 km^3 (bulk volume) pyroclastic products dispersed towards the E–NE, followed by a phreatomagmatic phase during which fallout activity has alternated with minor pyroclastic density currents confined to the volcano slopes. The Plinian fallout deposit is characterized by a strong compositional variation from white trachytic pumices (0.34 km^3 DRE; Landi et al. 1999) to black latitic–shoshonitic scoriae (0.96 km^3 DRE); during this phase, the mass discharge rate remained stable in the range of $2–2.5 \times 10^7$ kg/s corresponding to a column height of 16–17 km (Bertagnini et al. 1998), despite the change towards mafic composition.

In this case study, the micro-textural features of clasts from the whole Pomici di Base Plinian fallout succession have been quantitatively investigated by generating high-resolution three-dimensional digital maps via X-ray computed microtomography. The obtained textural information (i.e., density measurements, bubble and throat number density and size distributions, bubble interconnectivity, etc.), combined with geochemical and Sr- and Nd-isotopic data on both separated groundmass and phenocrysts, has contributed to reconstruct the trigger mechanisms and conduit dynamics that controlled this Plinian eruption fed by a less evolved magma.

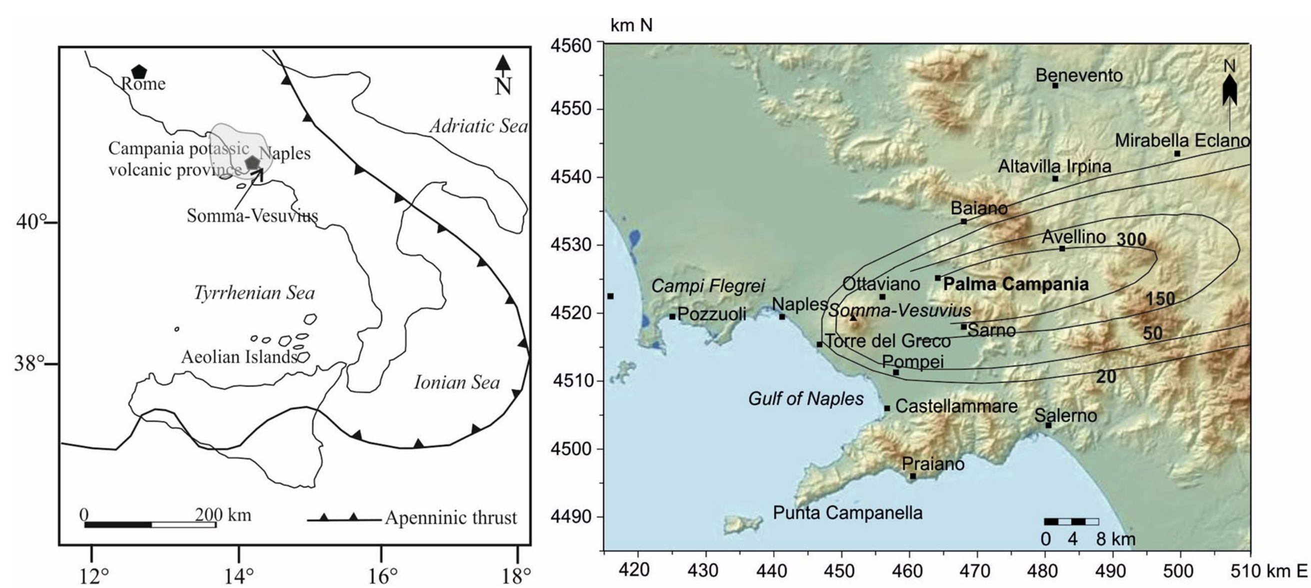

Fig. 1 On the left: location map for Somma–Vesuvius volcano (Italy), situated within Campanian Potassic Volcanic Province (gray field). On the right: distribution of Pomici di Base fallout unit (Bertagnini et al. 1998)

Sampling and methods

Representative juvenile pumice and scoria clasts of the entire Plinian fallout succession of the Pomici di Base eruption were collected from two key stratigraphic sections located at about 15 km NE of the Somma–Vesuvius (Palma Campania, near Naples), Fig. 1. The Plinian deposit is composed of a basal white pumiceous layer, overlain by a transitional gray pumice layer and an upper black scoria bed (Fig. 2). The three beds have an approximately constant relative thickness of 2:1:5 (Bertagnini et al. 1998). The sampling interval was dictated by changes in type, grain size, and color of the pyroclastic products, according to the different stratigraphic units recognized by Bertagnini et al. (1998), Fig. 2. Samples location within eruptive units is reported in Fig. 2.

Bulk density

To account for possible density variations with size, we used juvenile clasts within a −5 to −2 phi size range for density measurements. Sets of 100 clasts for each granulometric class (where present) were weighted and coated with a thin film of paraffin wax, and their density was determined using a pycnometer. We calculated bulk vesicularity for each clast following the procedure described in Houghton and Wilson (1989), using a dense-rock equivalent (DRE) density of 2700 (latite–shoshonite) and 2400 (trachyte) kg/m^3, obtained by pycnometry measurements on fine-grained whole-rock powder as described in ASTM (2007).

No differences in clast-density distributions have been observed between the analyzed granulometric classes. Moreover, juvenile clasts with different sizes and same density, accurately observed under optical microscope, show comparable textural features. However, to avoid any possible influence of post-fragmentation expansion, we have selected clasts within 4 and 8 mm size range, as larger clasts do not necessarily preserve the vesicularity of the magma immediately prior to fragmentation (e.g., Thomas et al. 1994; Gardner et al. 1996; Kaminski and Jaupart 1997).

Modal density clasts were selected from the base to the top of the deposits to investigate micro-textural variations with stratigraphic height (see also Gurioli et al. 2005; Balcone-Boissard et al. 2008, 2012; Houghton et al. 2010).

Microtomographic investigation

The microstructure of the samples was investigated by X-ray computed microtomography (micro-CT) using a Carl Zeiss Xradia Versa-410 3D X-ray microscope at the Istituto Nazionale di Geofisica e Vulcanologia—Sezione di Napoli "Osservatorio Vesuviano" (INGV-OV, Naples).

X-ray computed microtomography is a non-destructive analysis technique that offers the opportunity to visualize and quantify the internal structure of rock samples by generating three-dimensional digital maps with a very high resolution (down to submicron). Particularly, the result of microtomographic investigation is a three-dimensional gray-level image proportional to the X-ray attenuation coefficient of the sample (that for the same energy is a function of the density and atomic number of the interested material), which allows the observation and measurement of the properties of objects (e.g., shape, size, distribution, and orientation of fractures, pores, crystals, etc.) entirely avoiding the stereological corrections needed for measurements carried out in two dimensions.

Particularly, Xradia Versa architecture uses a two-stage magnification technique. First, a geometric magnification, as with conventional micro-CT, is obtained. In the second stage, a scintillator converts X-rays to visible light, which is then optically magnified. Reducing dependence upon geometric magnification enables Xradia Versa instruments to maintain submicron resolution at large working distances.

In this study, cylinders of maximum diameter 0.5 cm were cut from the samples and the scan was performed over a 360° rotation using 4001 projections, 80 KV voltage, and 10 W power. The resulting nominal voxel (volumetric pixel) size ranges from 0.9 to 2 µm depending on the optical magnification used (10X and 20X, see Table 1). However, imaging using any method (optical, SEM, XMT, etc.), where the smallest feature (vesicle or vesicle wall) is less than three pixels/voxels in diameter, is subject to significant uncertainty (Hughes et al. 2017). Therefore, we consider that the minimum measurable voxel size ranges from ≈ 3 to 6 µm (corresponding to 3 voxel size) as also confirmed by accurate visual inspection of slices.

Reconstruction of the attenuation data was performed through the filtered back-projection algorithm using XRM-Reconstructor Xradia proprietary software producing a stack of 967 cross-sectional, gray-scale digital images, Fig. 3.

3D and 2D textural measurements

Vesicle and throat size distributions and number densities were obtained by processing the 3D tomographic images. First, the obtained 3D micro-CT images were filtered using grayscale-to-grayscale filters available in Blob3D software (Ketcham 2005) to improve the brightness and contrast and to obtain an edge enhancement of the vesicles. Then, the 3D images were segmented to isolate vesicles from matrix glass and crystals on the basis of their gray-level values (thresholding), which are related to the X-ray

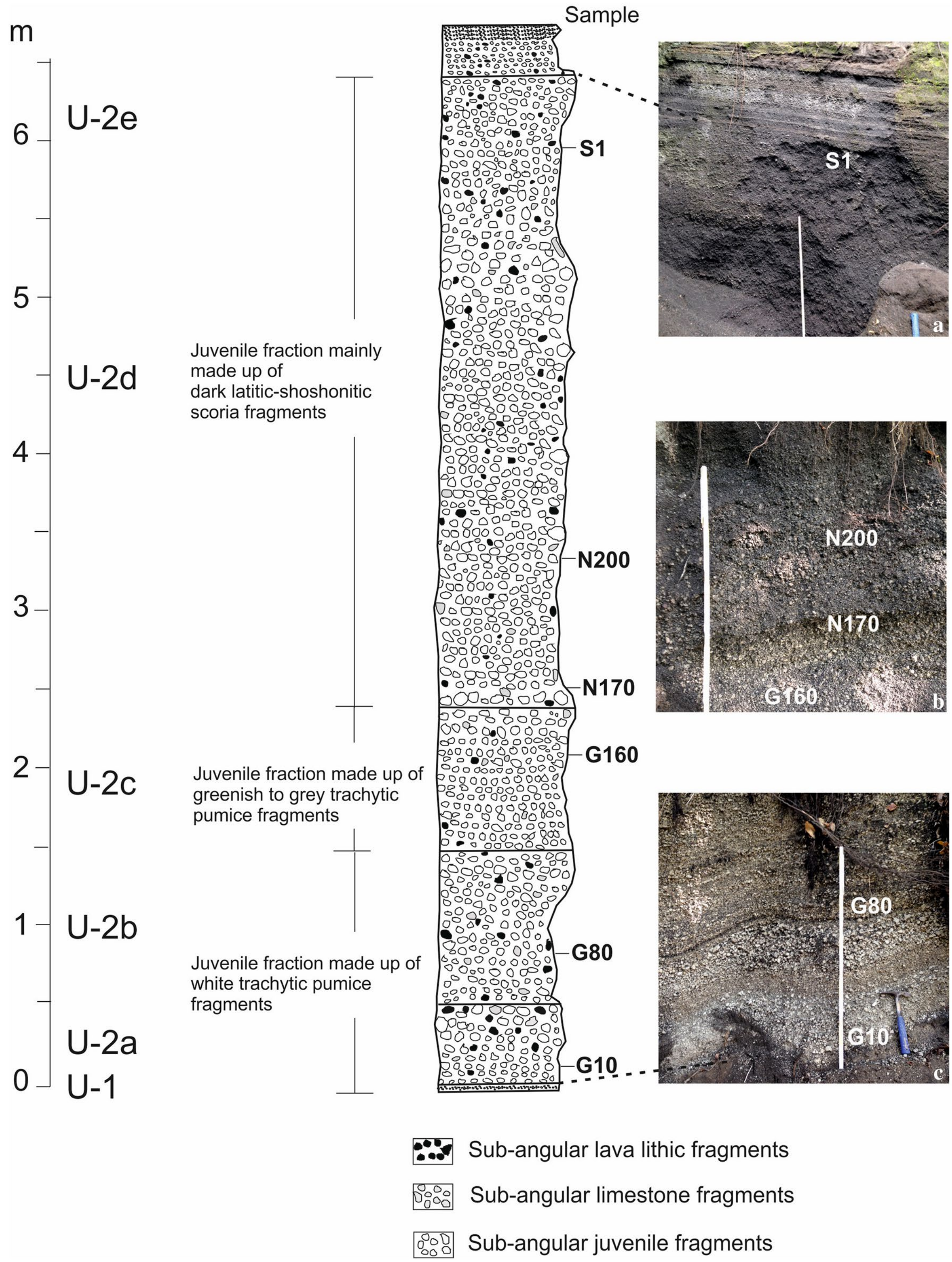

Fig. 2 Representative photos and schematic stratigraphic column for the Pomici di Base Plinian deposits and sample number for clasts collected for this study. Samples were collected from two stratigraphic sections (**a** and **b**–**c**, respectively, on the right). Sampling interval was dictated by changes in type, grain size, and color of the pyroclastic products, according to the different stratigraphic units recognized by Bertagnini et al. 1998 (on the left): U-1—ash and pumice fall deposits; U-2—Plinian fallout deposit composed by a basal white pumiceous layer (U-2a and U-2b), a transitional layer (U-2c), an upper thick black scoria bed (U-2d and U-2e); U-3—U-6 lithic-rich fallout and PDCs (pyroclastic surge and flow) deposits

Table 1 Textural parameters for Pomici di Base rocks

Sample	Modal density (g/cm^3)	Modal porosity (%)	Objective	Voxel size (µm)	Field of view (mm^3)	Vesicularity (%)	Vg/Vl	*Y*
G10	0.59	75	10×	2.01	5.28	73	3.22	0.999
G10	–	–	20×	1.07	0.83	81	5.37	0.999
G80	0.58	76	10×	2.01	5.37	74	3.23	0.999
G80	–	–	20×	1.07	0.83	87	8.99	0.999
G160	0.57	76	10×	2.00	5.28	75	3.46	0.999
G160	–	–	20×	1.07	0.83	81	5.27	0.999
N170	0.61	75	10×	1.41	1.83	69	2.46	0.999
N170	–	–	20×	1.09	0.89	74	3.16	0.999
N200	1.10	59	10×	1.87	4.26	55	0.73	0.992
N200	–	–	20×	1.09	0.89	59	1.54	0.996
S1	1.40	48	10×	2.02	5.36	53	1.18	0.996
S1	–	–	20×	0.94	0.56	58	1.46	0.990
Sample	Objective	VOI (mm^3)	Isolated/connected	*n* bubbles total	VND (m^3) meltcorr	Power law exp	R^2	VND* (m^{-3}) meltcorr
G10	10×	2.77	0.05	23571	3.74E+13	4.07	0.99	–
G10	20×	0.36	0.04	14308	2.62E+14	–	–	3.63E+14
G80	10×	3.14	0.02	24178	3.36E+13	5.05	0.97	–
G80	20×	0.46	0.08	10047	2.27E+14	–	–	3.5E+14
G160	10×	3.09	0.02	27496	4.08E+13	4.34	0.99	–
G160	20×	0.46	0.09	10436	1.47E+14	–	–	3.21E+14
N170	10×	1.07	0.03	20660	6.88E+13	4.98	0.98	–
N170	20×	0.49	0.13	15322	1.34E+14	–	–	3.11E+14
N200	10×	2.49	0.22	61815	4.42E+13	4.52	0.99	–
N200	20×	0.37	0.43	24342	1.70E+14	–	–	1.07E+15
S1	10×	3.14	0.28	31642	2.23E+13	3.99	0.99	–
S1	20×	0.31	2.21	39246	3.16E+14	–	–	2.88E+15
Sample	Objective	VOI (mm^3)	*n* throats	#th/#por (#th/#con)	TND (m^3) corr	Power law exp	R^2	*k* (m^2)
G10	10×	4.74	135130	2.08 (3.43)	8.59E+13	3.42	0.98	2.70E−12
G80	10×	5.37	228113	3.45 (4.67)	1.16E+14	5.27	0.97	1.42E−12
G160	10×	5.28	211709	3.59 (4.22)	1.18E+14	4.72	0.98	2.58E−12
N170	10×	1.83	151654	2.74 (5.17)	3.90E+14	5.02	0.98	4.09E−12
N200	10×	4.26	276023	1.84 (4.55)	1.21E+14	4.37	0.99	4.50E−13
S1	10×	5.36	101343	1.62 (3.04)	4.44E+14	3.27	0.95	8.90E−13

Vesicles' (VND) and throats' (TND) number density has been corrected for clast vesicularity and phenocrysts content

*Following Adams et al. 2006, VND values have been extended to 1 µm vesicle diameter size by extrapolating the exponential curve described by the small bubbles (Fig. 4)

attenuation coefficient. In particular, the automatic Otsu algorithm (Otsu 1979) was adopted, manually adjusting the threshold when necessary using ImageJ (Schneider et al. 2012) software (e.g., Okumura et al. 2008; Caricchi et al. 2011; Zandomeneghi et al. 2010; Voltolini et al. 2011; Berg et al. 2016). A further step involved the extraction of a volume of interest (VOI) with dimensions suitable for the available computing resources but preserving sample representativeness to separate the connected pores and restore the pre-fragmentation conditions. The VOI has to be larger than the Representative Elementary Volume (REV; Bear 1972), which corresponds to the smallest portion of the sample that statistically represents all features of the entire sample (e.g., Degruyter et al. 2010; Zandomeneghi et al. 2010; Berg et al. 2016; Kennedy et al. 2016). The determination of REV is estimated by an iterative process based on the calculation of porosity on increasing 3D image volumes until reaching a plateau value. Potential

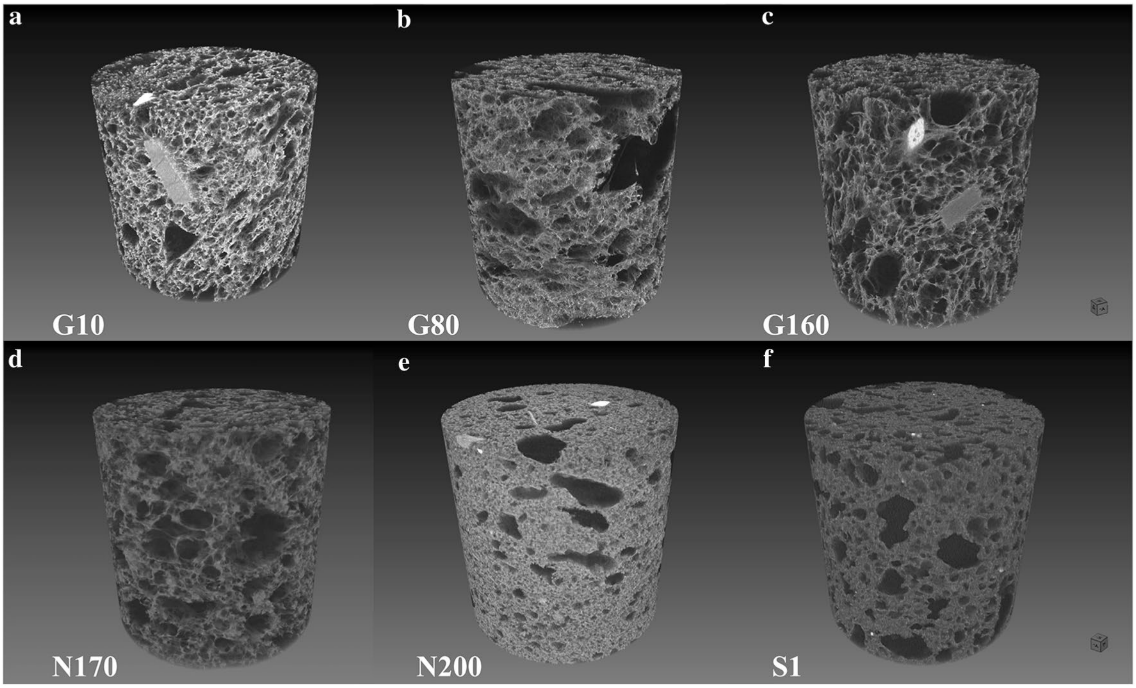

Fig. 3 Examples of volume rendering showing 3D microstructure of Pomici di Base trachytic (**a**–**d**) and latitic–shoshonitic (**e**–**f**) rocks. Cylinders diameter: 1000 µm. Vesicles are black, melt/feldspars/pyroxenes are gray, and oxides are white

cutting effects from sample preparation and artifacts of the cone–beam reconstruction were avoided by selecting VOIs in the central parts of the imaged volumes.

Connected vesicles have been separated reconstructing the thin glass films lost during image acquisition and processing or partially retracted in a late-stage of coalescence (Shea et al. 2010a; Giachetti et al. 2011; Rust and Cashman 2011; Hughes et al. 2017). Separations of connected vesicles were obtained using the Separate Objects tool available in Avizo FEI software based on a combination of watershed, distance map, and H-maxima. To quantitatively and graphically characterize pore interconnection, we adopted Pore Network Statistics Extension in Avizo FEI software. The obtained Pore Network Model (PNM, Fig. 4d) is composed of branching or endpoints of the network called pores (or vesicles for volcanic rock) and lines connecting pores called throats. The results of the different analyzed components (vesicles and throats) and their distributions are reported in Table 1. Volume rendering was obtained using Dragonfly ORS software.

Moreover, permeability measurement was carried out using Avizo FEI software (Petrophysics Extension), which contains the Absolute Permeability Experiment Simulation tool. Permeability has been calculated along the three orthogonal directions assuming a gas viscosity of 10^{-5} Pa s (Rust and Cashman 2011; Okumura et al. 2012).

Small density contrast between microlites (clinopyroxene and feldspar) and matrix glass has prevented a 3D quantitative investigation of microlites, for which conventional 2D analytical methods have been adopted.

Microlite crystallinity and size distributions were obtained by 2D Back-Scattered Electron images. For each sample, at least 4–5 BSE images (270 × 200 µm) were acquired by a Field Emission Scanning Electron Microscope (FE-SEM) JEOL JSM-6500F (Istituto Nazionale di Geofisica e Vulcanologia, Rome, Italy) and a Scanning Electron Microscope (SEM) Jeol JSM 5310 (DiSTAR, Università di Napoli Federico II) equipped with energy dispersive system and operating at 15 kV. BSE images were processed and analyzed using ImageJ software. They were first reduced to binary images and then manipulated to reduce noise and separate individual microlites. Microlite size distributions were obtained using CSD Corrections 1.5 program (Higgins 2000, 2002, 2006; Higgins and Chandrasekharam 2007) that includes corrections for both the intersection probability and the cut section effects.

Electron microprobe analyses (EMPA)

Analyses of major and volatile elements in groundmass glasses were performed with a JEOL-JXA-8200 electron microprobe (WD/ED combined microanalyzer) at the laboratories of the Istituto Nazionale di Geofisica e Vulcanologia (Rome). Element concentrations were measured with a 10 µm beam at 15 keV, a beam current of 10 Na, and a counting time of 10 s. For each analysis, a defocused beam was

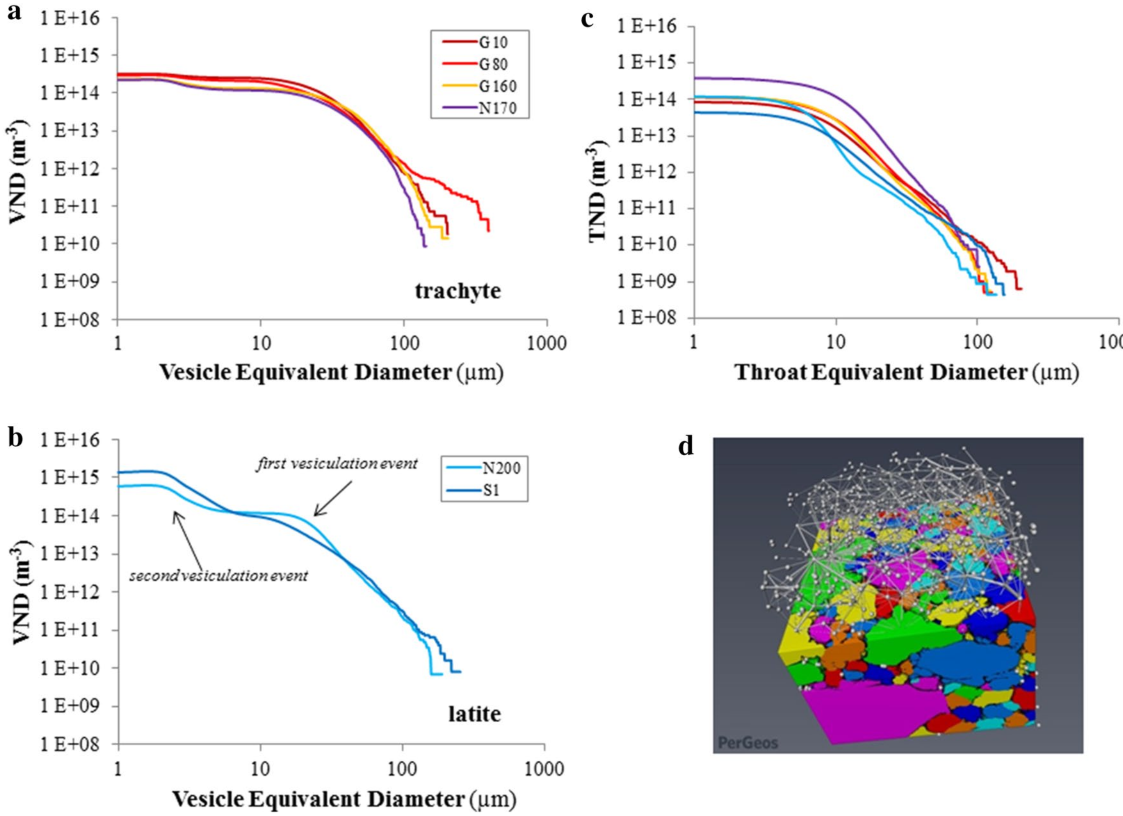

Fig. 4 Cumulative Vesicles size distributions (CVSDs) for trachytic (**a**) and latitic–shoshonitic (**b**) Pomici di Base rocks and Cumulative Throats size distributions (**c**). CVSDs of trachytic pumices show a curved continuous trend characterized by exponential distribution for the small bubbles and power-law distribution for the large bubbles, indicating a continuous nucleation process (see text). The presence of pre-existing bubbles in the upper gas-rich level of the chamber could justify the large bubble population observed in G80 sample. On the contrary, CVSDs of scoria latitic–shoshonitic samples show irregular trends formed by multiple curved segments suggesting discrete vesiculation events, attributed to nucleation pulses driven by fast CO_2 release during the ongoing decarbonation process (see text for further explanation). Example of Image of Pore Network Model (sample G10) obtained by Avizo FEI software (**d**). A PNM is composed of labeled branching or endpoints of the network called pores (or vesicles for volcanic rocks) and lines connecting pores called throats. Pores are displayed using spheres, and throats are displayed using cylinders. Cube side: 300 μm (pixel size = 1 μm)

used to minimize losses of alkalis and volatiles, which were counted first to avoid diffusion effects. The following standards have been adopted for the various chemical elements: jadeite (Si and Na), corundum (Al), forsterite (Mg), andradite (Fe), rutile (Ti), orthoclase (K), barite (Ba), celestine (S), fluorite (F), apatite (P and Cl), and spessartine (Mn). Data reduction was carried out using ZAF4/FLS software by Link Analytical. The analytical uncertainty was about 1 wt% for most elements. In a first attempt, the water content of all analyzed glass was estimated using the "volatile by difference" method based on EMPA analyses (Devine et al. 1995; King et al. 2002). EMPA data are reported in Table 2.

H_2O and CO_2 determination

Carefully selected natural pumice and scoria fragments were stored overnight in an H_2O_2 (20% in aqueous solution) bath to remove organic materials. Successively, the samples were left to dry in the air for 24 h and lately stored overnight in a drying oven at 110 °C to release water possibly adsorbed on the glass surface.

After this treatment, the H_2O–CO_2 contents in the scorias and in the pumices were analyzed with different methods at the Institute of Mineralogy at the University of Göttingen.

Water contents on bulk samples were measured by thermogravimetric analyses (TGA) using a SetaramTM TGA92. During a typical analyses, 10–20 mg of coarsely powdered material is loaded into a Pt crucible (4 mm diameter and 10 mm height) and covered with a Pt lid. The sample is heated from ambient temperature to 1200 °C with a ramp rate of 10°C/min. After 30 min dwell time, the sample is cooled to room temperature again with a cooling rate of 30 °C/min. In the case of iron poor samples, the measurements are performed in the air, while iron rich samples (FeO > 5 wt%) are measured in helium to avoid the oxidation of Fe^{2+} to Fe^{3+} by reaction with the dissolved water.

Table 2 EMPA analyses of selected Pomici di Base volcanic rocks

Samples	G10	G80	G160	N170	N200	S1
Number of analyzed points	8	8	9	8	10	6
SiO_2	61.68 (0.25)	61.59 (0.92)	60.01 (0.85)	60.25 (0.78)	57.24 (0.84)	55.44 (1.47)
TiO_2	0.32 (0.04)	0.29 (0.06)	0.35 (0.05)	0.39 (0.06)	0.53 (0.09)	0.71 (0.16)
Al_2O_3	17.66 (0.14)	17.41 (0.20)	17.60 (0.27)	17.72 (0.15)	18.28 (0.23)	17.34 (0.76)
FeO	2.56 (0.13)	2.59 (0.11)	3.23 (0.14)	3.21 (0.14)	4.71 (0.29)	7.00 (0.87)
MnO	0.17 (0.04)	0.15 (0.06)	0.15 (0.04)	0.12 (0.05)	0.15 (0.04)	0.16 (0.05)
MgO	0.24 (0.02)	0.25 (0.03)	0.46 (0.04)	0.47 (0.05)	0.96 (0.24)	1.34 (0.46)
CaO	2.49 (0.06)	2.67 (0.09)	3.27 (0.14)	3.21 (0.16)	4.77 (0.20)	4.85 (1.00)
Na_2O	4.36 (0.08)	3.83 (0.52)	3.89 (0.22)	4.00 (0.23)	3.32 (0.15)	3.31 (0.28)
K_2O	8.21 (0.20)	8.15 (0.18)	8.41 (0.37)	8.54 (0.23)	7.69 (0.15)	7.72 (0.41)
P_2O_5	0.07 (0.04)	0.06 (0.05)	0.12 (0.06)	0.09 (0.03)	0.31 (0.05)	0.62 (0.17)
Cl	0.71 (0.02)	0.68 (0.02)	0.55 (0.03)	0.57 (0.05)	0.54 (0.06)	0.64 (0.05)
F	0.24 (0.04)	0.21 (0.06)	0.20 (0.04)	0.18 (0.08)	0.19 (0.08)	0.22 (0.07)
SO_3	0.02 (0.01)	0.02 (0.02)	0.03 (0.01)	0.02 (0.01)	0.04 (0.02)	0.04 (0.02)
Total	98.72 (0.41)	97.88 (1.19)	98.27 (1.15)	98.75 (0.94)	98.73 (0.91)	99.38 (1.09)
H_2O by diff.	1.28 (0.41)	2.12 (1.19)	1.73 (1.15)	1.25 (0.94)	1.27 (0.91)	0.62 (1.09)
H_2O (TGA, wt%)	1.26 ± 10	2.57 ± 17	1.86 ± 9	1.31 ± 6	1.33 ± 14	0.68 ± 9
CO_2 (CSA, ppm)	1054 ± 170	788 ± 95	356 ± 35	1143 ± 100	268 ± 58	317 ± 135

During the analyses, the weight loss of the material is constantly recorded. Once a day, a final heating and cooling cycle is performed after a simple run to account for buoyancy changes dependent on the temperature of the sample and, therefore, to correct the measured sample weight loss (Schmidt and Behrens 2008).

For each sample, three-to-six thermogravimetric analyses were performed.

The determination of the CO_2 content on bulk samples was performed with an ElementarTM Inductar CS Cube Carbon–Sulfur Analyser (CSA). About 100–150 mg of coarsely crushed sample mixed with 0.5 g of Fe and 2 g of W chips are filled in a corundum crucible. After inductive firing, the mixture is burned in an oxygen stream releasing the CO_2 which is then measured with an IR cell. According to the manufacturer, a temperature of approx. 2000 °C is reached within 1 min.

Several steel samples with known carbon contents are used as standard calibration (Behrens et al. 2009).

Radiogenic isotopes

Isotopic analyses for Sr and Nd via thermal ionization mass spectrometry (TIMS) were carried out at the Istituto Nazionale di Geofisica e Vulcanologia—Sezione di Napoli "Osservatorio Vesuviano" (INGV-OV, Naples), using a ThermoFinnigan Triton TI multi-collector mass spectrometer. Samples were processed through conventional HF–HNO_3–HCl dissolution before Sr and middle REE (MREE) were separated by standard cation exchange column chemistry, and Nd was further purified on an anion column. Sr and Nd were then loaded onto Ta and Re filaments, respectively. Sr and Nd blanks were negligible for the analyzed samples during the periods of measurements. Measured $^{87}Sr/^{86}Sr$ ratios were normalized for within-run isotopic fractionation to $^{87}Sr/^{86}Sr = 0.1194$, and $^{143}Nd/^{144}Nd$ ratios to $^{143}Nd/^{144}Nd = 0.7219$. The mean measured value of $^{87}Sr/^{86}Sr$ for NIST–SRM 987 was 0.710215 ± 0.000008 (2 sigma, $n = 36$) and of $^{143}Nd/^{144}Nd$ for LaJolla was 0.511843 ± 0.000006 (2 sigma, $n = 11$). The quoted error is the standard deviation of the mean (2 sigma) for $n = 180$. Sr and Nd isotope ratios have been normalized to the recommended values of NIST SRM 987 ($^{87}Sr/^{86}Sr = 0.71025$) and La Jolla ($^{143}Nd/^{144}Nd = 0.51185$) standards, respectively. Results are reported in Table 3.

Results

Clast density, vesicularity, and crystallinity

All samples show less than 5 wt% content of phenocrysts that are present both as isolated crystals and in aggregate and are made up of sanidine > plagioclase > clinopyroxene > biotite in order of decreasing abundance, together with minor amount of amphibole, magnetite, and garnet.

Clast densities as well as the degree of vesicularity and microlite crystallinity vary progressively upward in the stratigraphic sequence, Table 1, similar to what previously observed by Bertagnini et al. (1998). In particular, the basal and intermediate (white to gray) trachytic pumices show

Table 3 Isotopic ratios of separated glass and minerals of Pomici di Base rocks

$^{87}Sr/^{86}Sr$	Glass		Minerals			
Samples		2sigma	Sanidine	2sigma	Pyroxene	2sigma
G10	0.707527	±6	0.707499	±6	0.707500	±6
G80	0.707530	±7	–		–	
G160	0.707539	±6	0.707550	±6	0.707477	±6
N170	0.707556	±8	0.707506	±6	0.707470	±6
N200	0.707602	±6	–		–	
S1	0.707605	±7	0.707534	±6	–	±6
$^{143}Nd/^{144}Nd$	Glass		Minerals			
Samples		2sigma	Sanidine	2sigma	Pyroxene	2sigma
G10	0.512439	±7	–		0.512437	±7
G80	0.512447	±7	–		–	
G160	0.512432	±6	0.512440	±6	0.512444	±6
N170	0.512435	±6	0.512429	±7	0.512452	±6
N200	0.512436	±6	–		–	
S1	0.512431	±6	–		0.512452	±7

low-density modal values (0.57–0.61 g/cm^3), high vesicularity (69–87%), and absence of microlites, while the upper (black) latitic–shoshonitic scoriae are characterized by higher density values (1.1–1.5 g/cm^3) and poorly vesiculated (45–59%) microlite-rich groundmass. Bulk vesicularities calculated by pycnometry are generally consistent with those obtained by the 3D images at lower 10× magnification (see Table 1), while the values slightly increase in high-resolution three-dimensional images; however, the dissimilarity is always less than 15% as also observed by Giachetti et al. (2011) using a similar procedure for Vulcanian pyroclasts erupted from Montserrat.

Two vesicle populations characterize highly vesiculated trachytic pumices: small (diameter < 25 μm) spherical bubbles and irregular-shaped large bubbles (> 25 μm) showing many stages of coalescence (Fig. 3a–d and supplementary movie 1). Particularly, large bubbles have smooth pore apertures or interstitial filaments between coalesced cavities. In these cases, melt films between bubbles can be very thin, reaching a 1 μm minimum thickness. This corresponds to the inferred critical thickness of liquid film rupture (Cashman and Mangan 1994) that, in the case of equally sized bubbles, is suggested to be caused by approximately equal pressure acting on the film from inside each bubble (Klug et al. 2002). Concurrently, small bubbles present wrinkled melt retraction films, possible in response to release of gas overpressure (Adams et al. 2006). Poorly vesiculated latitic–shoshonitic scoriae have different textures that are predominantly characterized by small bubble population (< 40 μm) and subordinately by large polylobate, amoeboid bubbles separated by thick (> 10 μm) microlite-bearing glass (Fig. 3e, f, and supplementary movie 2).

Microlite types are small (< 5–150 μm) blocky clinopyroxene in the lower part of scoriaceous level (15 vol%, N200 sample) joined to elongated plagioclase in the upper scoria samples (30 vol%, S1 sample).

Vesicle number density and size distributions

Textures of pyroclasts, specifically the Vesicle Number Density (VND) and Size Distribution (VSD), can be quantified from image analyses (see Methods) and used to constrain processes and conditions of magma decompression during the course of the eruption (e.g., Cashman and Mangan 1994; Mangan and Cashman 1996; Hammer et al. 1999). Particularly, VND (number of vesicles per volume unit) is potentially a powerful tool to explore rates of magma ascent because of the relationship between number density and decompression rate observed in laboratory experiments as well as numerical models, while VSDs are largely used to constrain the processes of bubbles nucleation, growth, and coalescence and then to investigate the relationships between magma degassing and eruptive behavior (e.g., Gaonac'h et al. 1996; Blower et al. 2002; Toramaru 2006; Proussevitch et al. 2007a, b).

Table 1 includes VND values calculated by using all the micro-CT images acquired at different resolutions; however, as suggested by other authors (Shea et al. 2010a, b; Rotella et al. 2014), we consider the VND data measured from the higher resolution micro-CT images more representative as small bubbles dominate the bubble density in silicic pyroclasts. Moreover, following the method proposed by Adams et al. (2006) for the 1912 eruption of Novarupta, VND values have been extended to 1 μm vesicle diameter size by extrapolating the exponential curve described by the small bubbles. Particularly, following the last authors, we fitted the trend of smaller bubbles with an exponential curve and extended it to 1 µm vesicle diameter size. As in the case of 1912 eruption of Novarupta, for our trachytic pumice samples, the exponential size distribution corresponds to vesicles ≤ 30–25 µm, while for our scoria samples, the exponential trend fits vesicles smaller than 10–15 µm.

VNDs are quite similar for all trachytic pumice clasts collected at different stratigraphic levels ranging from 3.1 to 3.6×10^{14} m^{-3}, while increase in latitic–shoshonitic scoria samples at the top of the deposit that show VND values up to 2.8×10^{15} m^{-3}, Table 1. The obtained VND values are consistent with those produced by heterogeneous nucleation during decompression experiments on Neapolitan trachytes (4.8×10^{13}–2.9×10^{14} m^{-3}; Mastrolorenzo and Pappalardo 2006) and phonolites (4.3×10^{13}–3.8×10^{14} m^{-3}; Larsen 2008; 8×10^{13}–9×10^{15} m^{-3}; Shea et al. 2010b), as well as those produced by homogeneous nucleation on phonolites (5.7×10^{14}–7.7×10^{14} m^{-3}; Iacono-Marziano et al. 2008).

Cumulative vesicle size distributions (CVSDs) of trachytic pumices show a continuous trend characterized by an exponential distribution for small bubbles (less than 25 µm) and a power-law distribution for large bubbles (Fig. 4a). Similar trends have been observed in other Plinian events and widely interpreted as due to expansion and coalescence of earlier formed vesicles (large bubbles' pattern) during a continuous nucleation process (Gaonac'h et al. 1996; Blower et al. 2002), while the small bubbles reflect the last nucleation event in the shallow conduit (e.g., Baker et al. 2012; Gonnermann and Houghton 2012; Rotella et al. 2014).

On the contrary, CVSDs of scoria samples show irregular trends formed by multiple curved segments suggesting discrete vesiculation events (Fig. 4b). These sorts of distributions are generally not typical of Plinian clasts; however, they have been previously recognized in experimental samples that suffered carbonate interaction and explained as due to vesiculation pulses triggered by fast release of CO_2-rich fluids (Blythe et al. 2015). Interestingly, it is the first time that these trends have been observed in natural Somma–Vesuvius rocks, possibly thanks to the high-resolution of the applied 3D microtomographic technique (examples of 3D micro-CT data for trachytic and latitic–shoshonitic rocks are in supplementary movies 1 and 2, respectively).

Number density and size distribution of throats, connectivity, and permeability

Total Throats Number Densities (TNDs) range from 8.6×10^{13} to 4.4×10^{14} m^{-3}, not showing substantial differences between latitic–shoshonitic scoriae and trachytic pumices, Table 1. The ratio between numbers of throats/total pores (#th/#por in Table 1) and throats/connected pores (#th/#con) ranges, respectively, from 2.1 to 3.6 and 3.4 to 5.2 in trachyte and 1.6 to 1.8 and 3 to 4.5 in latite–shoshonite. Their cumulative distributions (CTSDs, Cumulative Throats Size Distributions) follow broadly power-law trends for large sizes, while seem to follow exponential trends for the small sizes, similar to those observed in the vesicle size distributions of trachytic pumice, Fig. 4c. These observations are consistent with the fact that bubble growth in pumices is better developed than in scoriae, resulting in thinner melt films, which facilitate the occurrence of coalescence process between neighboring vesicles (e.g., higher #th/#por in trachyte with respect to latite). Moreover, they reflect the high number of small isolated vesicles contained in scoriae, characterized by different CVSDs' trends. The degree of bubble interconnection has been evaluated based on bubble connectivity by the procedures described in Okumura et al. (2012). Connectivity is defined as $\Psi = N_{max}/N_{total}$ (where N_{max} and N_{total} represent the voxel numbers belonging to the largest bubble and to all of the bubbles, respectively) and reaches the very high value of about 0.99 in all samples. Permeability values (see Methods) range from 1.42 to 4.09×10^{-12} m^2 for trachytic pumices and from 0.45 to 0.89×10^{-12} m^2 for latitic–shoshonitic scoriae, without showing significant variations among the three orthogonal directions (Table 1).

Microlite size distributions

Following the pioneering work of Marsh (1988) and Cashman and Marsh (1988), the size of microlites and their abundance can be represented as Crystal Size Distributions (CSDs), generally shown as a semi-logarithmic plot of population density (number of crystals per unit volume) vs crystal size (maximum length) with the slope equal to 1/(growth rate × residence time). Thus, if the growth rate is known, the crystallization time can be computed.

CSDs for clinopyroxene present in the glassy groundmass of our latitic–shoshonitic samples were obtained by textural analyses of 2D back-scattered electron images; however, it was not possible to analyze plagioclase crystals as their average atomic mass is close to that of the surrounding matrix glass; thus, they cannot be quantitatively resolved in the BSE images.

These distributions show intercept and slope values of 17.69 and 19.31 mm^{-4} and − 63 and − 93.2 mm^{-1} (for N200 and S1 samples, respectively, Fig. 5a). Because decompression experiments indicate that the growth rate of microlites can be highly dependent on the decompression rate, in our timescale calculations, we used the entire

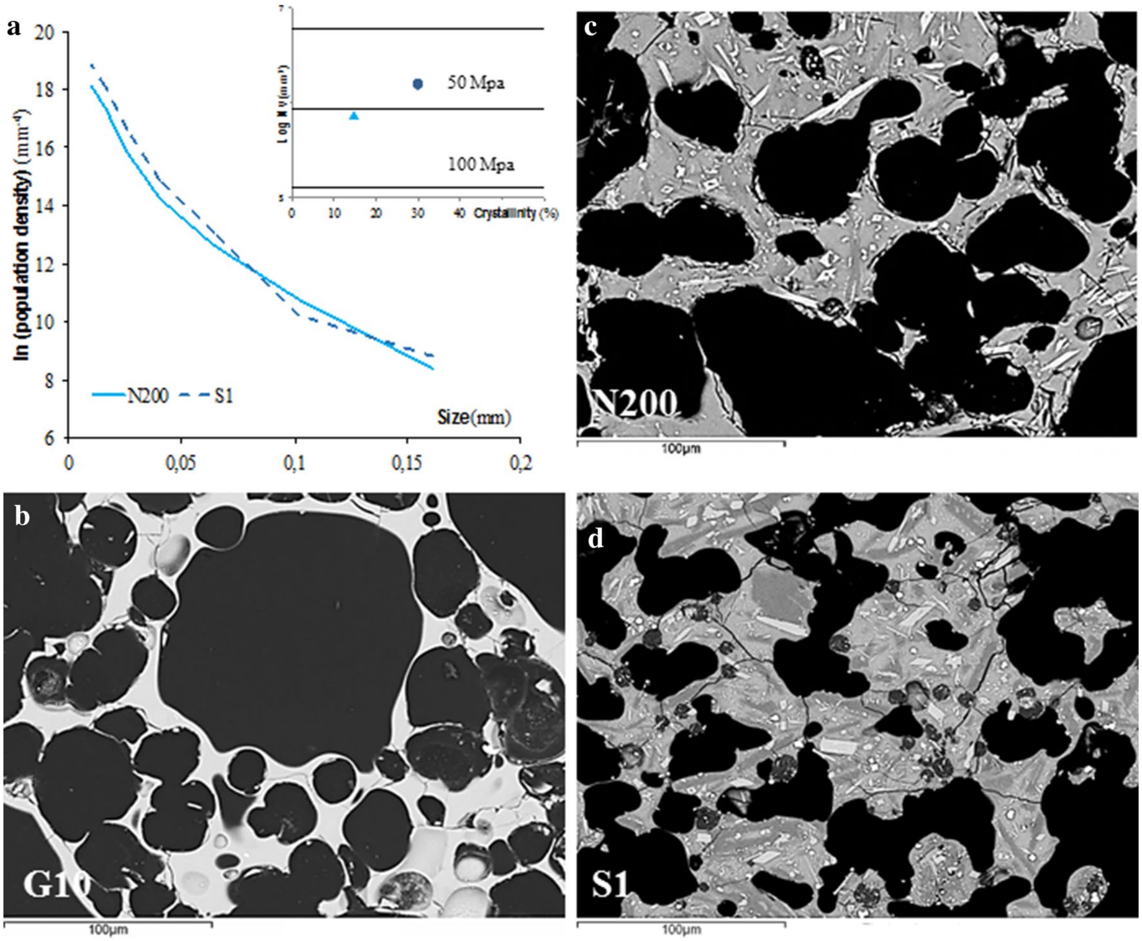

Fig. 5 **a** Crystal size distributions for clinopyroxene microlites (white microcrystals in BSE images). Insert: microlite number volume (Nv) against crystallinity showing microlite formation depths. These must be considered gross estimates as the equilibrium lines are calibrated on the basis of experimental rhyolitic samples (Blundy and Cashman 2008). Back-scattered electron (BSE) images of groundmass textural features in Pomici di Base trachytic (**b**) latitic–shoshonitic (**c** and **d**) samples

range of growth rates (from 1×10^{-6} to 1×10^{-8} mm/s, Brugger and Hammer 2010) available for microlites. By applying this range of growth rates, we calculated a crystallization time ranging from hours to days, in agreement with clinopyroxene texture displaying elongate, tabular, and swallowtail morphologies that indicate rapid crystallization close to the surface (Fig. 5).

Radiogenic isotope

To explore the potential influence of limestone assimilation in the evolution of the Pomici di Base magmas, we performed Sr–Nd-isotopic analyses on separated phenocrysts (feldspar and clinopyroxene) and groundmass in all studied samples. Radiogenic systems are in fact a powerful tool to spot magma contamination, due to the different Sr- and Nd-isotopic signatures of primary magmas with respect to crustal rocks.

The obtained results show a marked increment in $^{87}Sr/^{86}Sr$ ratios from trachytic (0.70753–56) to latitic–shoshonitic melts (0.70760) (Fig. 6a; Table 3), thus suggesting a prominent involvement of crustal contamination in the petrogenesis of the hotter mafic melts (Tliquidus = 1200 °C, calculated using MELTS program; Ghiorso and Sack 1995; Asimov and Ghiorso 1998), as also supported by the abundance of carbonate–metamorphic clasts present as lithic fraction in the Pomici di Base fallout deposits and included as fragments inside juvenile products (Bertagnini et al. 1998; Landi et al. 1999). Particularly, the highest $^{87}Sr/^{86}Sr$ ratios have been measured in separated latitic–shoshonitic glassy groundmass (0.70760) with respect to sanidine (0.70750–55) and clinopyroxene (0.70747–50) phenocrysts implying that contamination

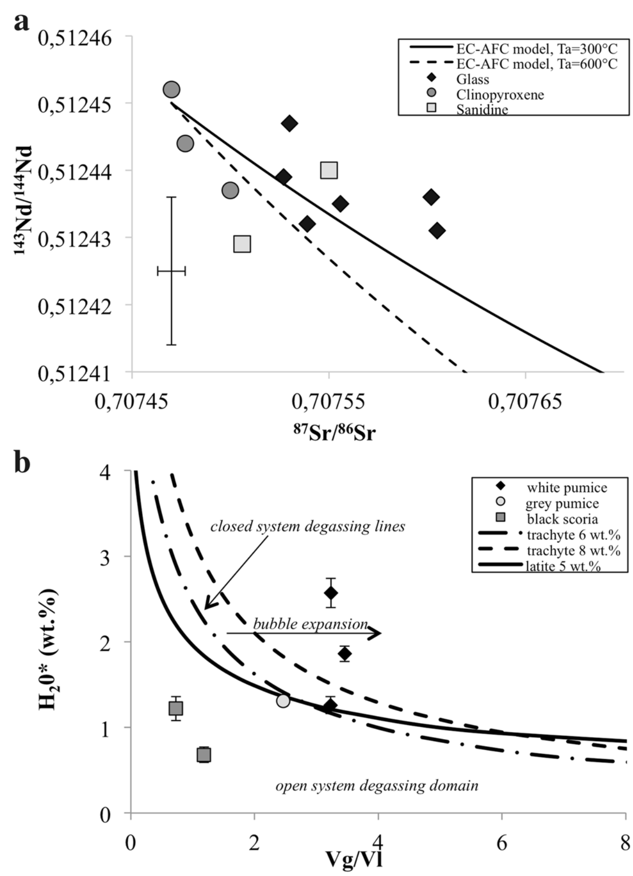

Fig. 6 **a** $^{87}Sr/^{86}Sr$ vs $^{143}Nd/^{144}Nd$ compositions for separated matrices and minerals. Lines represent the results of energy-constrained assimilation and fractional crystallization (EC–AFC; Spera and Bohrson 2001) simulations (see text for further explanations). Ta = initial T assimilant. **b** H_2O^* (water in residual melts) vs Vg/V_l (ratio of the volume of gas (Vg) to the volume of melts (V_l), after Balcone-Boissard et al. 2008). Lines correspond to theoretical closed-system degassing evolution for initial water content of 5 wt% (latite–shoshonite), 6 and 8 wt% (trachyte), representative of saturation conditions (Di Matteo et al. 2004, 2006)

was a later process occurred possibly at shallow level after precipitation of phenocrysts, Fig. 6a.

In other volcanic contexts, partial/selective assimilation has been advocated to explain isotopic disequilibrium between groundmass and feldspars (e.g., Duffield and Ruiz 1998); however, in the case of Pomici di Base rocks, this feature is restricted to mafic melts, while it is not significant in evolved trachyte, thus excluding that fractionation was coupled to a continuous selective assimilation process.

Nd-isotopic compositions are much less variable and cluster around 0.51243–45 both in matrix glasses and in phenocrysts (Fig. 6a), this in agreement with the low Nd content of sedimentary carbonates that leave a very slight fingerprint in the contaminated magmas.

The effects of assimilation on isotope variations have been modeled using the Energy-Constrained Assimilation and Fractional Crystallization (EC-AFC) model of Spera and Bohrson (2001), Table 4. We consider an early intrusion of a primitive shoshonitic magma at a liquidus temperature of 1200 °C into the upper crust at 350–600 °C ambient temperature (De Lorenzo et al. 2006) and 6–8 km depth supposed to be the top of the magma reservoir (Scaillet et al. 2008; Pappalardo and Mastrolorenzo 2010, 2012; Balcone-Boissard et al. 2016), possibly developed inside carbonatic sequences as suggested by borehole (Brocchini et al. 2001) and geophysical investigations (e.g., Berrino et al. 1998; Improta and Corciulo 2006). The model shows that the observed Sr- and Nd-isotopic variation is justified by 2–4% of carbonate rocks contaminating a magma already crystallized for about 55% of its initial mass, Fig. 6a.

Table 4 EC-AFC parameters used for modeling isotopic trend

Thermal parameters		Compositional parameters		
Liquidus T magma	1200 °C	Element	Sr	Nd
Initial T magma	1200 °C	Magma conc. (ppm)	1039	45.5
Liquidus T assimilant	1000 °C	Bulk D_m	1.6	0.1
Initial T assimilant	300–600 °C	Assimilant conc. (ppm)	500	10
Solidus	780 °C	Bulk D_a	0.7	0.15
Equilibrium temperature	900 °C			
Specific heat of magma	1484 J/Kg/K			
Specific heat of assimilant	1370 J/Kg/K	Isotope	$^{87}Sr/^{86}Sr$	$^{143}Nd/^{144}Nd$
Enthalpy of cryst. of magma	396,000 J/Kg	Ratio magma	0.70747	0.51245
Enthalpy of melting of ass.	270,000 J/Kg	Ratio assimilant	0.709	0.512

In the model, melts temperature was calculated using Melts program. An ambient temperature of 350 and 600 °C was assigned to crustal rocks consistent with mid-crustal magma storage. The liquidus (T_{la} = 1000 °C) and solidus (T_{sa} = 780 °C) temperatures for limestone are from Mollo et al. 2010. Bulk distribution coefficient for Sr and Nd is from Villemant et al. 1988; Pappalardo et al. 2008; Gebauer et al. 2014

Dynamics of magma ascent in the volcanic conduit

The Plinian fallout phase of the Pomici di Base eruption was fed in its early beginning by sialic (0.34 km^3 DRE trachytic) melts followed by a larger volume of mafic (0.96 km^3 DRE latitic–shoshonitic) magmas for the entire course of the sustained-column phase. This chemical variation towards mafic composition was not associated with any changes in eruption style, as flow rate as well as column height remained firmly high (Bertagnini et al. 1998) for tens of hours during the whole Plinian phase.

However, our 2D and 3D quantitative textural data and isotopic ratios show a significant difference between sialic and mafic rocks suggesting contrasting degassing as well as crystallization regime during magma ascent and fragmentation in the volcanic conduit.

Bubble nucleation and growth recorded in microlite-free trachytic pumice

Trachytic pumices have high degree of vesiculation (69–87%) and are characterized by large coalescent bubbles separated by thin glass walls, whose thickness approaches the critical rupture threshold. These features, commonly observed in pumice samples of Plinian eruptions from worldwide volcanoes (e.g., Rotella et al. 2014 and reference therein), allow us to hypothesize that during decompression, bubble growth occurred for exsolution up to the achievement of a vesicularity threshold that for silicic melts generally ranges from 70 to 80% in function of magma characteristics (expansion rate, melt viscosity, shear stresses, and presence of different phases). Above this value, experimental data (Namiki and Manga 2008; Takeuchi et al. 2009; Rust and Cashman 2011) indicate the existence of an abrupt increase in permeability due to bubbles coalescence. High throat number densities, power-law exponents > 3 in CVSDs as well as high bubble connectivity and permeability values of trachytic pumice also support extended bubble coalescence during magma ascent.

On the basis of the numerical model developed by Toramaru (2006), we estimated the decompression rate during this eruptive stage using the VND values calculated for pumice samples, surface tension of 0.1 N/m (Iacono Marziano et al. 2007; Mangan and Sisson 2000; Moutada Bonnefoi and Laporte 2004), 6 wt% pre-eruptive H_2O content at saturation pressure of 150–200 MPa (Di Matteo et al. 2004), and water diffusivity of 2.41×10^{-12} m^2/s. This last value has been calculated using the empirical equation proposed by Fanara et al. (2013) at 1100 °C (minimum experimental temperature adopted by the authors) and a correction factor of 100 to take into account the influence of the temperature (scaling from 1100 to 900 °C; following Watson 1994; Larsen 2008; Shea et al. 2010b). The resulting decompression rate is in the order of 5.5–6.1 MPa/s; however, these values must be considered maximum values as the used formulation does not take into account the role of pre-eruptive magmatic CO_2 in the melt that may influence water solubility at saturation.

The obtained high decompression rate implies that during the climax of this early phase of the eruption, magma degassing occurred rapidly under closed-system regime (see also Fig. 6b) from a storage depth of 150–200 MPa (Pappalardo et al. 2004; Scaillet et al. 2008; Pappalardo and Mastrolorenzo 2010, 2012; Balcone-Boissard et al. 2016) up to the fragmentation surface localized at ≤ 40 MPa, as inferred on the basis of residual water content of glass (Fig. 6b). At this point, the viscosity of trachytic magmas shifted from $10^{2.9}$ to $10^{4.91}$ Pa s (average values assuming saturation conditions for pre-eruptive stage and $T = 900$ °C, calculated using the model of Giordano et al. 2010).

Moreover, some pumice clasts show evidence of expansion without further water exsolution (Fig. 6b), a degassing regime that may correspond to the expansion of pre-existing bubbles in the chamber, despite we cannot completely exclude post-fragmentation vesiculation. We consider, however, the first hypothesis more plausible, because this feature is limited to the very first erupted trachytic products that represent the upper gas-rich level in the chamber possibly at critical conditions of volatile oversaturation; the occurrence of hydrous minerals (such as biotite) in the phenocryst assemblage supports crystallization under hydrous melt conditions; and in fact, crystallization experiments on alkaline trachytic melts (e.g., Fabbrizio and Carroll 2008) indicate that biotite instead of amphibole is stable as hydrous phase in alkaline trachytic compositions due to the high K_2O/Na_2O ratios of these melts. We speculate that the presence of melts in near-saturation conditions at the top of the chamber could act as an eruption trigger generating an excess pressure (5–25 MPa, following Blake 1984) sufficient to cause the wall-rock rupture.

Bubble and microlite nucleation and growth recorded in microlite-rich latitic–shoshonitic scoriae

Latitic–shoshonitic scoriae erupted in the late Plinian fallout stage, on the counterpart, are characterized by poorly vesicular texture (45–59%) as well as thick microlite-rich (crystallinity between 15 and 30 vol%) interstitial glass.

These features imply low magma ascent rate favoring open-system degassing regime (outgassing) and in turn bubble collapse as well as degassing-induced microlite crystallization (see also Figs. 5, 6b). On the other hand, a peculiar aspect of these rocks is their high vesicle number density and multiple CVSDs patterns, in contrast with their low-porosity and high-crystallinity nature. Similar behavior (high

VND values and CVSDs distributions) has been previously observed in experimental mafic samples from Somma–Vesuvius and Merapi volcanoes exposed to limestone contamination (Blythe et al. 2015) and presumed due to fast (hours to days, Sottili et al. 2009, 2010; Deegan et al. 2010, 2011; Freda et al. 2011; Troll et al. 2012; Jolis et al. 2013) CO_2 nucleation pulses. This last process can be possibly driven by magma digestion of skarn blocks detached by contact aureole formed during an early magma-limestone metamorphic stage (skarn recycling, Jolis et al. 2015). Although we did not observe clear evidence of metasomatic nodules in our juvenile fragments, possibly due to their rare occurrence; Landi et al. (1999) reported the presence, within juvenile clasts, of metasomatic carbonates/skarn nodules (< 0.2 wt% of the total rock) commonly associated with interstitial trachytic glass interpreted as portions of the metasomatized carbonate walls of the upper part of the Pomici di Base magma chamber. In any case, we cannot exclude that magma/wall-rock interaction would involve also CO_2-rich pristine limestone.

Hence, we suggest that a mechanism of carbonate/skarn dissolution can reconcile all the 2D and 3D textural as well as isotopic parameters documented in Pomici di Base mafic rocks. We propose that the evacuation of the more evolved trachytic liquids from the cap of the reservoir has caused the inception of caldera collapse with the consequent digestion/assimilation of carbonate/skarn blocks into the remnant latitic–shoshonitic liquids, Fig. 7.

Specifically, we suggest that the widening of the lower part of the plumbing system causes a reduced magma ascent rate giving more time both to gas to escape (outgassing) and to microlite to grow, with a consequent increment of melt viscosity ($10^{4.43-7.48}$ Pa s, average values calculated on the basis of the model proposed by Vona et al. (2011), assuming an equilibrium temperature of 1000 °C). In fact, decompression experiments (e.g., Rutherford and Gardner 2000; Hammer and Rutherford 2002; Couch et al. 2003; Martel and Schmidt 2003) demonstrated that number density and modal content of microlites change accordingly to decompression rate and that microlite crystallization requires timescales of days to weeks, while it can be absent in the case of fast magma ascent.

This stage of conduit collapse as well as the associated phase of slow magma ascent through the conduit, possibly

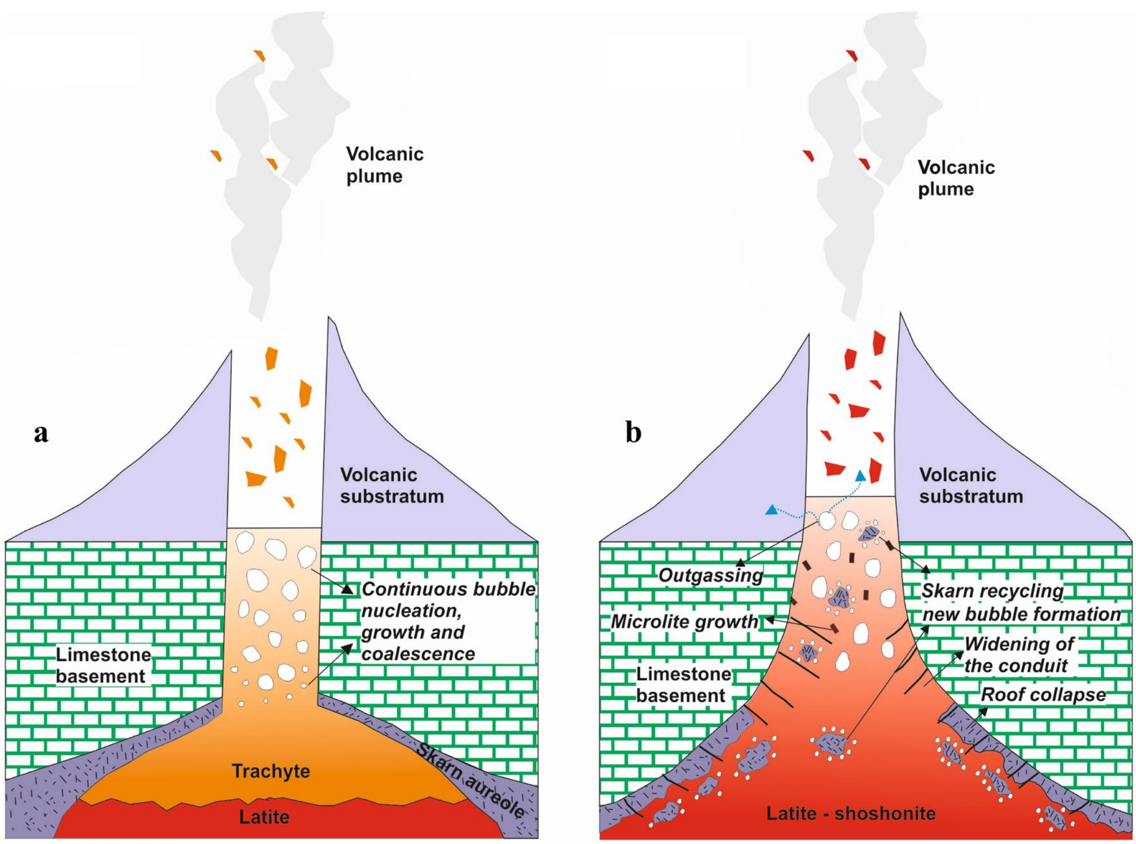

Fig. 7 Schematic model for conduit processes during the Plinian phase of Pomici di Base eruption. The fast evacuation of the more evolved trachytic liquids from the cap of the reservoir, caused the inception of the collapse of the deeper part of the plumbing system and the digestion/assimilation of skarn blocks into the remnant hotter latitic–shoshonitic liquids

lasted from hours to days as indicated by our CSDs data on clinopyroxene microlite. During this time, the consequent digestion/assimilation of carbonate/skarn blocks triggered CO_2 bubble formation and growth, forcing rising and fragmentation of the more viscous magma. Dallai et al. (2001) reported that the occurrence of CO_2 degassing due to the interaction of hot magma with carbonate has the potential to change the overall volatile solubility of magmas, thus justifying their ability to rapidly rise and explosively erupt to the surface. Recently Carr et al. (2018) by applying a numerical model of magma ascent to 2006 Merapi eruption, found that the addition of 1000 ppm of CO_2 can reduce water solubility in the melt, forcing vesiculation and generating overpressure at the top of the storage region in a short time (1–2 days).

Our EC-AFC simulations indicate the ingestion of 2–4 wt% of limestone by 0.96 km^3 (Landi et al. 1999) of latitic–shoshonitic melts that corresponds to the release of a maximum of 0.04 Gt of CO_2 during the eruption (considering that for 1 kg of limestone, 439 g of CO_2 are liberated for complete decarbonation, Deer et al. 1992). Similar values of CO_2 liberation are reported during the AD 79 Pompeii (0.31–0.56 Gt) and the AD 472 Pollena (0.04–0.07 Gt) eruptions at Somma–Vesuvius (Jolis et al. 2015).

The fragmentation mechanisms

Trachytic magma

In high-viscous magma, fragmentation occurs when (1) a critical viscosity-dependent strain rate is exceeded (strain-rate criterion; Papale 1999); (2) gas overpressure overcomes the tensile strength of the melt (stress criterion; Alidibirov 1994; Zhang 1999); or (3) expanding magma exceeds a critical vesicularity (critical volume fraction criterion; Sparks 1978).

The *strain-rate criterion* is based on the view that rapid acceleration may cause the melt to cross the glass transition and, therefore, fail brittlely. Papale (1999) indicates that magmas fragment in a brittle fashion when a critical, viscosity-dependent strain rate is exceeded. The minimum bulk viscosity (μ) required for strain-induced fragmentation is defined as $\mu \geq (CG_\infty \pi r^3/Q)^{(1/0.9)}$, where r is the conduit radius (m), Q is the volume flux (m^3/s), G_∞ is the elastic modulus at infinite frequency (10 GPa), and C is a fitting parameter (0.01 $(Pa\ s)^{-0.1}$) (Gonnermann and Manga 2003). Thus, to verify this criterion for the studied trachyte, we used in the above formulation the known mass flux for Pomici di Base eruption of $Q = 2.5 \times 10^7$ kg/s (Bertagnini et al. 1998) (equivalent to a volume flux of $Q = 10^4$ m^3/s) and the calculated average viscosity for trachytic melt ($10^{4.91}$ Pa s); however, the obtained conduit radius results around 1 m and thus geologically unrealistic.

The stress criterion establishes that fragmentation takes place when volatile overpressure, ΔP_{fr}, exceeds the tensile strength of the melt and ruptures bubble walls (Alidibirov 1994; Zhang 1999). Spieler et al. (2004) provide a formulation with good fit to a broad range of experimental data: $\Delta P_{fr} = \sigma_m/\varphi$, where σ_m is the effective tensile strength of the melt (0.995 MPa) and φ is the porosity. This formulation has been modified by Mueller et al. (2008) to account for permeability (k) as follows: $\Delta P_{fr} = (a\ k^{1/2} + \sigma_m)/\varphi$, with $a = 8.21 \times 10^5$ MPa/m and $\sigma_m = 1.54$ MPa, respectively. Thus, applying in the above formulations the measured porosity and permeability for trachyte melt (0.75 and 2.7×10^{-12} m^2), a bubble overpressure ranging from 1.33 to 3.85 MPa is required to cause fragmentation. As the calculated melt viscosity gives relaxation times (τ_s) of 8.13×10^{-6} s using the expression $\tau_s = \mu_s/G_\infty$ (Dingwell and Webb 1989), then the onset of non-Newtonian, un-relaxed, viscoelastic behavior can be fixed at 8.13×10^{-4} s (2 orders of magnitude below, Webb 1997). The above calculated ΔP_{fr} (1.33–3.85 MPa) and timescale (8.13×10^{-4} s) implies unrealistic huge decompression rates (comprised between 1.63 and 4.74×10^3 MPa/s) needed to initiate fragmentation.

The *critical volume fraction criterion* is thought to arise from some form of instability within the thin bubble walls, once $\phi \approx 0.75$ is reached (Verhoogen 1951; Sparks 1978). At high bubble-interconnectivity condition, the fragmentation efficiency strongly depends on the balance between rate of magma decompression and rate at which gases escape from the rising magma (outgassing). Okumura et al. (2012) have estimated the rate of outgassing from magmas ascending in volcanic conduits on the basis of Darcy's law and using the calculated gas permeability for silicic melts. This author reports that when the pressure gradient driving the permeable gas flow is assumed to be lithostatic (0.03 MPa m^{-1}), as can be postulated on the basis of the results of numerical models for silicic magma ascent during Plinian eruptions (Papale and Dobran 1993), the gas velocity is estimated to be less than 10^{-5} m/s at vesicularities up to 70 vol%. As this velocity is much smaller than the decompression rate (5.5–6.1 MPa/s) calculated by VND values in the previous "Bubble and microlite nucleation and growth recorded in microlite-rich latitic–shoshonitic scoriae", the degree of outgassing can be considered inefficient on the timescale of the eruption, thus allowing the reaching of the 0.75% porosity threshold necessary for fragmentation also in presence of high bubbles connectivity.

We can hence suppose that fragmentation of trachytic magma can occur after bubble expansion when a fixed gas volume threshold is reached (bubble packing state) as also suggested by Mastrolorenzo and Pappalardo (2006) on the basis of a compositional and textural study on both experimental and natural trachytes from Campania volcanoes.

Latitic–shoshonitic magma

In low-viscous liquids, fragmentation can be controlled by inertia due to inertial stretching and hydrodynamic breakup during rapid bubble growth.

Actually, the examined scoria clasts lack the textural features typical of low-viscous inertia-driven fragmentation products (fluidal shapes, very low VND values etc), possibly due to the large increment in melt viscosity caused by outgassing and microlite precipitation processes that affected mafic melts during magma rise in the conduit. On the other hand, the calculated high viscosity values suggest that brittle fragmentation can be a possible mechanism for latitic–shoshonitic melts.

To verify this hypothesis, we applied the mass flux measured for Pomici di Base eruption and the calculated viscosity values for latitic–shoshonitic compositions ($10^{4.43–7.48}$ Pa s) in the expression of Gonnerman and Manga (2003) for strain-induced brittle fragmentation (strain-rate criterion); a wide range of conduit radius values from 0.31 to 171.73 m results from calculation in function of viscosity variation depending on microlite content (ranging from 15 to 30 vol%). Indeed, our 3D data show only localized bubble deformation in mafic scoriae, implying that strain localization (Wrigth and Weinberg 2009) can occur during magma rising in the conduit, and force melts to cross the glass transition and achieve the fragmentation.

Moreover, calculations taking into account other fragmentation mechanisms (stress criterion and critical volume fraction criterion) give a wide range of decompression rates that can reach also extreme values (from 6.68–15.95 to $0.63–1.32 \times 10^4$ MPa s^{-1}) and vesicularity values significantly larger compared with those measured in the studied natural samples. It is noteworthy that in these calculations, we have neglected the contribution of CO_2-oversaturation condition possibly derived by the postulated limestone assimilation.

Finally, we speculate that latitic–shoshonitic magmas cannot reach classically defined fragmentation conditions and complex mechanisms such as bubble overpressure driven by CO_2 oversaturation (see also Pichavant et al. 2013) and strain localization can concur.

Conclusions

In this paper, we show that a combination of textural and petro-chemical quantification of the eruptive products can be a powerful tool for reconstructing volcanic conduit dynamics during volcanic eruptions. Our 2D and 3D quantitative textural data combined with Sr- and Nd-isotopic investigations demonstrated that explosive behavior during the Pomici di Base Plinian eruption was first controlled by rapid decompression under closed-system degassing regime of the uppermost trachytic liquids; subsequently, the inception of the caldera collapse triggered the digestion of detached skarn blocks into the remnant latitic–shoshonitic liquids and in turn the occurrence of rapid vesiculation pulses that contributed to magnify the intensity of the eruption during the evacuation of the mafic liquids.

To conclude, these results highlight the importance of magma/limestone interaction as a syn-eruptive process able to produce vigorous gas liberation, thus accelerating magma ascent and amplifying eruption intensity. This mechanism of CO_2 fast liberation warrants more detailed consideration as a mechanism driving explosive basaltic volcanism.

Acknowledgements The authors wish to thank I. Arienzo (INGV-OV), R. de Gennaro (Università di Napoli) and M. Nazzarini (INGV-Rome) for essential helps during isotopic, SEM and EMPA analyses, respectively. We are thankful to Ciro Sepe (DiSTAR, Università di Napoli) for his fundamental support during fieldwork. Finally, the authors gratefully acknowledge two anonymous reviewers, whose valuable suggestions greatly contributed to improve the manuscript.

Compliance with ethical standards

Conflict of interest The authors declare no competing financial interests.

References

Adams NK, Houghton BF, Hildreth W (2006) Abrupt transitions during sustained explosive eruptions: examples from the 1912 eruption of Novarupta, Alaska. Bull Volcanol 69:189–206

Alidibirov M (1994) A model for viscous magma fragmentation during volcanic blasts. Bull of Volcanol 56:459–465. https://doi.org/10.1007/s004450050055

Andronico D, Calderoni G, Cioni R, Sbrana A, Sulpizio R, Santacroce R (1995) Geological map of Somma–Vesuvius volcano. Per Min 64(1–2):77–78

Asimov PD, Ghiorso MS (1998) Algorithmic modifications extending MELTS to calculate subsolidus phase relations. Am Miner 83:1127–1132

ASTM Designation D854-06 (2007) Standard test method for specific gravity of soil solids by water pycnometer: annual book of ASTM standards, 04.02, ASTM, West Conshohocken, PA

Baker DR, Brun F, O'Shaughnessy C, Mancini L, Fife JL, Rivers M (2012) A four-dimensional X-ray tomographic microscopy study of bubble growth in basaltic foam. Nat Commun 3:1135

Balcone-Boissard H, Villemant B, Boudon G, Michel A (2008) Non-volatile vs volatile behaviours of halogens during the AD 79 Plinian eruption of Mt. Vesuvius, Italy. Earth Planet Sci Lett 269:66–79

Balcone-Boissard H, Villemant B, Boudon G (2010) Behavior of halogens during the degassing of felsic magma. Geochem Geophys Geosyst 11:477–485

Balcone-Boissard H, Boudon G, Ucciani G, Villemant B, Cioni R, Civetta L, Orsi G (2012) Magma degassing and eruption dynamics of the Avellino pumice Plinian eruption of Somma–Vesuvius (Italy). Comparison with the Pompeii eruption. Earth Planet Sci Lett 331–332:257–268

Balcone-Boissard H, Boudon G, Cioni R, Webster JD, Zdanowicz G, Orsi G, Civetta L (2016) Chlorine as a geobarometer for alkaline magmas: evidence from a systematic study of the eruptions of Mount Somma–Vesuvius. Sci Rep 6:21726

Bear J (1972) Dynamics of fluid in porous media. Elsevier, New York

Behrens H, Misiti V, Freda C, Vetere F, Botcharnikov RE, Scarlato P (2009) Solubility of H_2O and CO_2 in ultrapotassic melts at 1200 and 1250 °C and pressure from 50 to 500 MPa. Am Mineral 94:105–120

Berg SE, Troll VR, Deegan FM, Burchardt S, Krumbholz M, Mancini L, Polacci M, Carracedo JC, Soler V, Arzilli F, Brun F (2016) Heterogeneous vesiculation of 2011 El Hierro xeno-pumice revealed by X-ray computed microtomography. Bull Volcanol 78:85. https://doi.org/10.1007/s00445-016-1080-x

Berrino G, Corrado G, Riccardi U (1998) Sea gravity data in the Gulf of Naples: a contribution to delineating the structural pattern of the Vesuvian area. J Volcanol Geoth Res 82:139–150

Bertagnini A, Landi P, Rosi M, Vigliargio A (1998) The Pomici di Base Plinian eruption of Somma–Vesuvius. J Volcanol Geotherm Res 83:219–239

Blake S (1984) Volatile oversaturation during the evolution of silicic magma chambers as an eruption trigger. J Geophys Res 89:8237–8244

Blower JD, Keating JP, Mader HM, Phillips JC (2002) The evolution of bubble size distributions in volcanic eruptions. J Volcanol Geotherm Res 120(1–2):1–23

Blundy J, Cashman K (2008) Petrologic reconstruction of magmatic system variables and processes. Rev Mineral Geochem 69:179–239

Blythe LS, Deegan FM, Freda C, Jolis EM, Masotta M, Misiti V, Taddeucci J, Troll VR (2015) CO_2 bubble generation and migration during magma–carbonate interaction. Contrib Mineral Petrol 169(4):1–16. https://doi.org/10.1007/s00410-015-1137-4

Brocchini DC, Principe D, Castradori M, Laurenzi A, Gorla L (2001) Quaternary evolution of the southern sector of the Campanian Plain and early Somma–Vesuvius activity: insights from the Trecase 1 well. Mineral Petrol 73:67–91

Brugger CR, Hammer JE (2010) Crystal size distribution analysis of plagioclase in experimentally decompressed hydrous rhyodacite magma. Earth Planet Sci Lett 300:246–254

Caricchi L, Pommier A, Pistone M, Castro J, Burgisser A, Perugini D (2011) Strain-induced magma degassing: insights from simple-shear experiments on bubble bearing melts. Bull Volcanol 73:1245. https://doi.org/10.1007/s00445-011-0471-2

Carr BB, Clarke AB, de' Michieli Vitturi M (2018) Earthquake induced variations in extrusion rate: a numerical modeling approach to the 2006 eruption of Merapi Volcano (Indonesia). Earth Planet Sci Lett 482:377–387

Cashman KV, Mangan MT (1994) Physical aspects of magmatic degassing; II, Constraints on vesiculation processes from textural studies of eruptive products. In: Carroll M (ed) Volatiles in magma. Mineral Soc Am, Washington, DC, pp 447–478

Cashman K, Marsh B (1988) Crystal size distribution (CSD) in rocks and the kinetics and dynamics of crystallization II. Makaopuhi lava lake. Contrib Mineral Petrol 99:292–305

Cioni R, Bertagnini A, Santacroce R, Andronico D (2008) Explosive activity and eruption scenarios at Somma–Vesuvius (Italy): towards a new classification scheme. J Volcanol Geotherm Res 178:331–346

Cnudde V, Boone MN (2013) High-resolution X-ray computed tomography in geosciences: a review of the current technology and applications. Earth Sci Rev 123:1–17

Cole PD, Scarpati C (2010) The 1944 eruption of Vesuvius, Italy: combining contemporary accounts and field studies for a new volcanological reconstruction. Geol Mag 147:391–415

Couch S, Sparks RSJ, Carroll MR (2003) The kinetics of degassing induced crystallization at Soufrie`re Hills volcano, Montserrat. J Petrol 44:1477–1502

Cubellis E, Marturano A, Pappalardo L (2016) The last Vesuvius eruption in March 1944: reconstruction of the eruptive dynamic and its impact on the environment and people through witness reports and volcanological evidence. Nat Hazards 82:95. https://doi.org/10.1007/s11069-016-2182-7

Dallai L, Cioni R, Boschi C, D'Oriano C (2011) Carbonate-derived CO_2 purging magma at depth: influence on the eruptive activity of Somma–Vesuvius, Italy. Earth Planet Sci Lett 310:84–95

De Lorenzo S, Di Renzo V, Civetta L, D'Antonio M, Gasparini P (2006) Thermal model of the Vesuvius magma chamber. Geophys Res Lett 33:L17302

De Vivo B, Petrosino P, Lima A, Rolandi G, Belkin HE (2010) Research progress in volcanology in the Neapolitan area, southern Italy: a review and some alternative views. Mineral Petrol 99:1–28

Deegan FM, Troll VR, Freda C, Misiti V, Chadwick JP, McLeod CL, Davidson JP (2010) Magma-carbonate interaction processes and associated CO_2 release at Merapi volcano, Indonesia: insights from experimental petrology. J Petrol 51:1027–1051

Deegan FM, Troll VR, Freda C, Misiti V, Chadwick JP (2011) Fast and furious: crustal CO_2 release at Merapi volcano, Indonesia. Geol Today 27:57–58

Deer WA, Howie RA, Zussman J (1992) An introduction to the rock-forming minerals. Longman Scientific and Technical, 2nd ed. Wiley, New York

Degruyter W, Bachmann O, Burgisser A (2010) Controls on magma permeability in the volcanic conduit during the climactic phase of the Kos Plateau Tuff eruption (Aegean Arc). Bull Volcanol 72(1):63. https://doi.org/10.1007/s00445-009-0302-x

Delibrias G, Di Paola GM, Rosi M, Santacroce R (1979) La storia eruttiva del complesso vulcanico Somma-Vesuvio ricostruita dalle successioni piroclastiche del Monte Somma. Rend Soc It Mineral Petrol 35:411–438

Devine JD, Gardner JE, Brack HP, Layne GD, Rutherford MJ (1995) Comparison of analytical methods for estimating H_2O contents of silicic volcanic glasses. Am Mineral 80:319–328

Di Matteo V, Carroll MR, Behrens H, Vetere F, Brooker RA (2004) Water solubility in trachytic melts. Chem Geol 213:187–196

Di Matteo V, Mangiacapra A, Dingwell DB, Orsi G (2006) Water solubility and speciation in shoshonitic and latitic melt composition from Campi Flegrei Caldera (Italy). Chem Geol 229(1–3):113–124

Dingwell DB, Webb S (1989) Structural relaxation in silicate melts and non-Newtonian melt rheology in geologic processes. Phys Chem Miner 16(5):508–516. https://doi.org/10.1007/BF00197020

Duffield WA, Ruiz J (1998) A model that helps explain Sr-isotope disequilibrium between feldspar phenocrysts and melt in largevolume silicic magma systems. J Volcanol Geotherm Res 87:7–13

Fabbrizio A, Carroll MR (2008) Experimental constraints on the differentiation process and pre-eruptive conditions in the magmatic system of Phlegrean Fields (Naples, Italy). J Volcanol Geotherm Res 171:88–102

Fanara S, Behrens H, Zhang Y (2013) Water diffusion in potassium-rich phonolitic and trachytic melts. Chem Geol 346:149–161

Freda C, Gaeta M, Giaccio B, Marra F, Palladino DM, Scarlato P, Sottili G (2011) CO_2-driven large mafic explosive eruptions: The Pozzolane Rosse case study from the Colli Albani Volcanic

District (Italy). Bull Volcanol 73(3):241–256. https://doi.org/10.1007/s00445-010-0406-3
Gaonac'h H, Lovejoy S, Stix J, Schertzer D (1996) A scaling growth model for bubbles in basaltic lava flows. Earth Planet Sci Lett 139:395–409
Gardner JE, Thomas RME, Jaupart C, Tait S (1996) Fragmentation of magma during Plinian volcanic eruptions. Bull Volcanol 58:144–162
Gebauer SK, Schmitt AK, Pappalardo L, Stockli DF, Lovera OM (2014) Crystallization and eruption ages of Breccia Museo (Campi Flegrei caldera, Italy) plutonic clasts and their relation to the Campanian ignimbrite. Contrib Mineral Petrol 167(1):1–18
Ghiorso MS, Sack RO (1995) Chemical mass transfer in magmatic processes IV. A revised and internally consistent thermodynamic model for the interpolation and extrapolation of liquid-solid equilibria in magmatic systems at elevated temperatures and pressures. Contrib Miner Petrol 119:197–212
Giachetti T, Burgisser A, Arbaret L, Druitt TH, Kelfoun K (2011) Quantitative textural analysis of Vulcanian pyroclasts (Montserrat) using multi-scale X-ray computed microtomography: comparison with results from 2D image analysis. Bull Volcanol 73:1295–1309
Giordano D, Polacci M, Papale P, Caricchi L (2010) Rheological control on the dynamics of explosive activity in the 2000 summit eruption of Mt. Etna Solid Earth 1:61–69. https://doi.org/10.5194/se-1-61-2010
Gonnermann HM, Houghton BF (2012) Magma degassing during the Plinian eruption of Novarupta, Alaska, 1912. Geochem Geophys Geosyst 13:Q10009. https://doi.org/10.1029/2012GC00427
Gonnermann HM, Manga M (2003) Explosive volcanism may not be an inevitable consequence of magma fragmentation. Nature 426:432–435. https://doi.org/10.1038/nature02138
Gurioli L, Houghton BF, Cashman KV, Cioni R (2005) Complex changes in eruption dynamics during the 79AD eruption of Vesuvius. Bull Volcanol 67:144–159
Gurioli L, Harris AJL, Houghton BF, Polacci M, Ripepe M (2008) Textural and geophysical characterization of explosive basaltic activity at Villarrica volcano. J Geophys Res 113:B08206
Hammer J, Rutherford MJ (2002) An experimental study of the kinetics of decompression-induced crystallization in silicic melt. J Geophys Res 107:1–24
Hammer JE, Cashman KV, Hoblitt RP, Newman S (1999) Degassing and microlite crystallization during pre-climactic events of the 1991 eruption of Mt, Pinatubo, Philippines. Bull Volcanol 60:355–380
Higgins MD (2000) Measurement of crystal size distributions. Am Mineral 85:1105–1116
Higgins MD (2002) Closure in crystal size distributions (CSD), verification of CSD calculations, and the significance of CSD fans. Am Mineral 87:171–175
Higgins MD (2006) Quantitative textural measurements in igneous and metamorphic petrology. Cambridge University Press, Cambridge
Higgins MD, Chandrasekharam D (2007) Nature of sub-volcanic magma chambers, Deccan province, India: evidence from quantitative textural analysis of plagioclase megacrysts in the Giant Plagioclase Basalts. J Petrol 48:885–900
Houghton BF, Wilson CJN (1989) A vesicularity index for pyroclastic deposits. Bull Volcanol 51:451–462
Houghton BF, Carey RJ, Cashman KV, Wilson CJN, Hobden BJ, Hammer JE (2010) Diverse patterns of ascent, degassing, and eruption of rhyolite magma during the 1.8 ka Taupo eruption, New Zealand: evidence from clast vesicularity. J Volcanol Geotherm Res 195:31–47
Hughes EC, Neave DA, Dobson KJ, Withers PJ, Edmonds M (2017) How to fragment peralkaline rhyolites: observations on pumice using combined multi-scale 2D and 3D imaging. J Volcanol Geotherm Res 336:179–191
Iacono-Marziano G, Gaillard F, Pichavant M (2007) Limestone assimilation and the origin of CO_2 emissions at the Alban Hills (Central Italy): constraints from experimental petrology. J Volcanol Geotherm Res 166:91–105
Iacono-Marziano G, Gaillard F, Pichavant M (2008) Limestone assimilation by basaltic magmas: an experimental re-assessment and application to Italian volcanoes. Contrib Mineral Petrol 155:719–738
Improta L, Corciulo M (2006) Controlled source nonlinear tomography: a powerful tool to constrain tectonic models of the Southern Apennines orogenic wedge, Italy. Geology 34:941–944
Jerram DA, Higgins MD (2007) 3D analysis of rock textures: quantifying igneous microstructures. Elements 3:239–245
Jolis EM, Freda C, Troll VR, Deegan FM, Blythe LS, McLeod CL, Davidson JP (2013) Experimental simulation of magma–carbonate interaction beneath Mt. Vesuvius, Italy. Contrib Mineral Petrol 166(5):1335–1353
Jolis EM, Troll VR, Harris C, Freda C, Gaeta M, Orsi G, Siebe C (2015) Skarn xenolith record crustal CO_2 liberation during Pompeii and Pollena eruptions, Vesuvius volcanic system, central Italy. Chem Geol 415:17–36. https://doi.org/10.1016/j.chemgeo.2015.09.003
Kaminski E, Jaupart C (1997) Expansion and quenching of vesicular magma fragments in Plinian eruptions. J Geophys Res 102:12817–12203
Kennedy BM, Wadsworth FB, Vasseur J, Schipper CI, Jellinek AM, von Aulock FW, Hess KU, Russell JK, Lavallée Y, Nichols ARL, Dingwell DB (2016) Surface tension driven processes densify and retain permeability in magma and lava. Earth Planet Sci Lett 433:116–124
Ketcham RA (2005) Computational methods for quantitative analysis of three-dimensional features in geological specimens. Geosphere 1(1):32–41
King PL, Venneman TW, Holloway JR, Hervig RL, Lowenstern JE, Forneris JF (2002) Analytical techniques for volatiles: A case study using intermediate (andesitic) glasses. Am Mineral 87:1077–1089
Klebesz R, Bodnar RJ, De Vivo B, Török K, Lima A, Petrosino P (2012) Composition and origin of nodules from the ~ 20 ka Pomici di Base (PB)-Sarno eruption of Mt. Somma–Vesuvius, Italy. Centr Eur J Geosci 4(2):324–337
Klebesz R, Esposito R, De Vivo B, Bodnar RJ (2015) Constraints on the origin of sub-effusive nodules from the Sarno (Pomici di Base) eruption of Mt. Somma–Vesuvius (Italy) based on compositions of silicate-melt inclusions and clinopyroxene. Am Mineral 100(4):760–777
Klug C, Cashman KV, Bacon C (2002) Structure and physical characteristics of pumice from the climactic eruption of Mount Mazama (Crater Lake), Oregon. Bull Volcanol 64:486–501
Landi P, Bertagnini A, Rosi M (1999) Chemical zoning and crystallization mechanisms in the magma chamber of the Pomici di Base Plinian eruption of Somma–Vesuvius (Italy). Contrib Mineral Petrol 135:179–197
Larsen JF (2008) Heterogeneous bubble nucleation and disequilibrium H_2O exsolution in Vesuvius K-phonolite melts. J Volcanol Geotherm Res 175:278–288
Lirer L, Petrosino P, Alberico I (2010) Hazard and risk assessment in a complex multisource volcanic area: the example of the Campania region, Italy. Bull Volcanol 72:411–429
Mangan MT, Cashman KV (1996) The structure of basaltic scoria and reticulite and inferences for vesiculation, foam formation, and fragmentation in lava fountains. J Volcanol Geotherm Res 73:1–18

Mangan M, Sisson T (2000) Delayed, disequilibrium degassing in rhyolite magma: decompression experiments and implications for explosive volcanism. Earth Planet Sci Lett 183:441–455

Marsh B (1988) Crystal size distribution (CSD) in rocks and the kinetics and dynamics of crystallization I. Theory. Contrib Mineral Petrol 99:277–291

Martel C, Schmidt BC (2003) Decompression experiments as an insight into ascent rates of silicic magmas. Contrib Mineral Petrol 144:397–415

Mastrolorenzo G, Pappalardo L (2006) Magma degassing and crystallization processes during eruptions of high-risk Neapolitan volcanoes: Evidence of common equilibrium rising processes in alkaline magmas. Earth Plan Sci Lett 250:164–181

Mastrolorenzo G, Pappalardo L (2010) Hazard assessment of explosive volcanism at Somma–Vesuvius. J Geophys Res 115:B12212

Mastrolorenzo G, Pappalardo L, Troise C, Panizza A, De Natale G (2008) Probabilistic tephra hazard maps for the Neapolitan area: quantitative volcanological study of Campi Flegrei eruptions. J Geophys Res 113:B07203. https://doi.org/10.1029/2007JB004954

Mollo S, Gaeta M, Freda C, Di Rocco T, Misiti V, Scarlato P (2010) Carbonate assimilation in magmas: a reappraisal based on experimental petrology. Lithos 114:503–514

Mourtada-Bonnefoi CC, Laporte D (2002) Homogeneous bubble nucleation in rhyolitic magmas: an experimental study of the effect of H_2O and CO_2. J Geophys Res 107:B4. https://doi.org/10.1029/2001JB00290

Mueller S (2007) Permeability and porosity as constraints on the explosive eruption of magma: laboratory experiments and field investigations. In: Earth and environment. Ludwig-Maximilians University, Munich, pp 1–149

Namiki A, Manga M (2008) Transition between fragmentation and permeable outgassing of low viscosity magmas. J Volcanol Geotherm Res 169:48–60

Okumura S, Nakamura M, Tsuchiyama A, Nakano T, Uesugi K (2008) Evolution of bubble microstructure in sheared rhyolite: formation of a channel-like bubble network. J Geophys Res 113:B07208

Okumura S, Nakamura M, Nakano T, Uesugi K, Tsuchiyama A (2012) Experimental constraints on permeable gas transport in crystalline silicic magmas. Contrib Mineral Petrol 164:493–504

Otsu N (1979) A threshold selection method from gray level histograms. IEEE Trans Syst Man Cybern 9:62–66. https://doi.org/10.1109/TSMC.1979.4310076

Papale P (1999) Strain-induced magma fragmentation in explosive eruptions. Nature 397:425–428. https://doi.org/10.1038/17109

Papale P, Dobran F (1993) Modeling of the ascent of magma during the plinian eruption of Vesuvius in A.D. 79. J Volcanol Geothermal Res 58:101–132

Pappalardo L, Mastrolorenzo G (2010) Short residence times for alkaline Vesuvius magmas in a multi-depth supply system: Evidence from geochemical and textural studies. Earth Plan Sci Lett 296:133–143

Pappalardo L, Mastrolorenzo G (2012) Rapid differentiation in sill-like magma reservoir: a case study from the Campi Flegrei caldera. Sci Rep 2:712. https://doi.org/10.1038/srep00712

Pappalardo L, Piochi M, Mastrolorenzo G (2004) The 3550 YR BP—1944 AD magma-plumbing system of Somma–Vesuvius, constraints on its behavior and present state through a review of Sr–Nd isotope data. Ann Geophys 47:1471–1483

Pappalardo L, Ottolini L, Mastrolorenzo G (2008) The Campanian Ignimbrite, Southern Italy. geochemical zoning, insight on the generation of a super-eruption from catastrophic differentiation and fast withdrawal. Contrib Mineral Petrol 156:1–26

Pappalardo L, D'Auria L, Cavallo A, Fiore S (2014) Petrological and seismic precursors of the paroxysmal phase of the last Vesuvius eruption on March 1944. Sci Rep 4:6297

Pichavant M, Di Carlo I, Rotolo SG, Scaillet B, Burgisser A, Le Gall N, Martel C (2013) Generation of CO_2-rich melts during basalt magma ascent and degassing. Contrib Mineral Petrol 166:545–561

Polacci M, Baker DR, Mancini L, Favretto S, Hill RJ (2009) Vesiculation in magmas from Stromboli and implications for normal Strombolian activity and paroxysmal explosions in basaltic systems. J Geophys Res 114:B01206

Polacci M, Baker DR, La Rue A, Mancini L, Allard P (2012) Degassing behaviour of vesiculated basaltic magmas: an example from Ambrym volcano, Vanuatu Arc. J Volcanol Geotherm Res 233– 234:55–64

Polacci M, Bouvet de Maisonneuve C, Giordano D, Piochi M, Mancini L, Degruyter W, Bachmann O (2014) Permeability measurements of Campi Flegrei pyroclastic products: an example from the Campanian Ignimbrite and Monte Nuovo eruptions. J Volcanol Geotherm Res 272:16–22. https://doi.org/10.1016/j.jvolgeores.2013.12.002

Proussevitch AA, Sahagian DL, Tsentalovich EP (2007a) Statistical analysis of bubble and crystal size distributions: formulations and procedures. J Volcanol Geotherm Res 164:95–111. https://doi.org/10.1016/j.jvolgeores.2007.04.007

Proussevitch AA, Sahagian DL, Carlson WD (2007b) Statistical analysis of bubble and crystal size distributions: application to Colorado Plateau basalts. J Volcanol Geotherm Res 164:112–126. https://doi.org/10.1016/j.jvolgeores.2007.04.006

Rotella MD, Wilson CJN, Barker SJ, Cashman KV, Houghton BF, Wright IC (2014) Bubble development in explosive silicic eruptions: insights from pyroclast vesicularity textures from Raoul volcano (Kermadec arc). Bull Volcanol 76:826

Rust AC, Cashman KV (2011) Permeability controls on expansion and size distributions of pyroclasts. J Geophys Res 116:B11202

Rutherford MJ, Gardner JE (2000) Rates of magma ascent. In: Sigurdsson H (ed) Encyclopedia of volcanoes. Academic Press, San Diego

Santacroce R, Cioni R, Marianelli P, Sbrana A, Sulpizio R, Zanchetta R, Donahued DJ, Joron JL (2008) Age and whole rock–glass compositions of proximal pyroclastics from the major explosive eruptions of Somma–Vesuvius: a review as a tool for distal tephrostratigraphy. J Volcanol Geotherm Res 177:1–18

Scaillet B, Pichavant M, Cioni R (2008) Upward migration of Vesuvius magma chamber over the past 20,000 years. Nature 455:216–219. https://doi.org/10.1038/nature07232

Scarpati C, Sparice D, Perrotta A (2016) Comparative proximal features of the main Plinian deposits (Campanian Ignimbrite and Pomici di Base) of Campi Flegrei and Vesuvius. J Volcanol Geoth Res 321:149–157

Scheibner B, Heumann A, Wörner G, Civetta L (2008) Crustal residence times of explosive phonolite magmas: U–Th ages of magmatic Ca-garnets of Mt. Somma–Vesuvius (Italy). Earth Planet Sci Lett 276:293–301. https://doi.org/10.1016/j.epsl.2008.09.028

Schmidt BC, Behrens H (2008) Water solubility in phonolite melts: influence of melt composition and temperature. Chem Geol 256:259–268

Schneider CA, Rasband WS, Eliceiri KW (2012) NIH Image to ImageJ: 25 years of image analysis. Nat Methods 9(7):671–675

Shea T, Houghton BF, Gurioli L, Cashman KV, Hammer JE, Hobden BJ (2010a) Textural studies of vesicles in volcanic rocks: an integrated methodology. J Volcanol Geotherm Res 190(3–4):271–289

Shea T, Gurioli L, Larsen JF, Houghton BF, Hammer JE, Cashman KV (2010b) Linking experimental and natural vesicle textures in Vesuvius 79 AD white pumice. J Volcanol Geotherm Res 192:69–84

Siani G, Sulpizio R, Paterne M, Sbrana A (2004) Tephrostratigraphy study for the last 18,000 14C years in a deep-sea sediment sequence for the South Adriatic. Quat Sci Rev 23:2485–2500

Song SR, Jones KW, Lindquist WB, Dowd BA, Sahagian DL (2001) Synchrotron X-ray computed microtomography: studies on vesiculated basaltic rock. Bull Volcanol 63:252–263

Sottili G, Taddeucci J, Palladino DM, Gaeta M, Scarlato P, Ventura G (2009) Sub-surface dynamics and eruptive styles of maars in the Colli Albani Volcanic District, Central Italy. J Volcanol Geotherm Res 180:189–202

Sottili G, Taddeucci J, Palladino DM (2010) Constraints on magma-wall rock thermal interaction during explosive eruptions from textural analysis of cored bombs. J Volcanol Geotherm Res 192:27–34

Sparks RSJ (1978) The dynamics of bubble formation and growth in magmas: a review and analysis. J Volcanol Geotherm Res 3:1–37. https://doi.org/10.1016/0377-0273(78)90002-1

Spera FJ, Bohrson WA (2001) Energy-constrained open-system magmatic processes I: general model and energy-constrained assimilation and fractional crystallization (EC-AFC) formulation. J Petrol 42:999–1018

Spieler O, Kenned B, Kueppers U, Dingwell DB, Scheu B, Taddeucci J (2004) The fragmentation threshold of pyroclastic rocks. Earth Planet Sci Lett 226:139–148. https://doi.org/10.1016/j.epsl.2004.07.016

Takeuchi S, Tomiya A, Shinohara H (2009) Degassing conditions for permeable silicic magmas: implications from decompression experiments with constant rates. Earth Planet Sci Lett 283(1–4):101–110

Thomas N, Jaupert C, Vergniolle S (1994) On the vesicularity of pumice. J Geophys Res 99:15,633–615,644

Toramaru A (2006) BND (bubble number density) decompression rate meter for explosive volcanic eruptions. J Volcanol Geotherm Res 154:303–316

Troll VR, Hilton DR, Jolis EM, Chadwick JP, Blythe LS, Deegan FM, Schwarzkopf LM, Zimmer M (2012) Crustal CO_2 liberation during the 2006 eruption and earthquake events at Merapi volcano, Indonesia. Geophys Res Lett 39:L11302. https://doi.org/10.1029/2012GL051307

Verhoogen J (1951) Mechanics of ash formation. Am J Sci 249:729–739

Villemant B (1988) Trace element evolution in the Phlegrean Fields Central Italy: fractional crystallization and selective enrichment. Contrib Mineral Petrol 98:169–183

Voltolini M, Zandomeneghi D, Mancini L, Polacci M (2011) Texture analysis of volcanic rock samples: quantitative study of crystals and vesicles shape preferred orientation from X-ray microtomography data. J Volcanol Geotherm Res 202:83–95

Vona A, Romano C, Dingwell DB, Giordano D (2011) The rheology of crystal-bearing basaltic magmas from Stromboli and Etna. Geochim Cosmochim Acta 75(11):3214–3236

Watson EB (1994) Diffusion in volatile-bearing magmas. Rev Mineral 30:371–411

Webb S (1997) Silicate melts: relaxation, rheology, and the glass transition. Rev Geophys 35(2):191–218

Wright HMN, Weinberg RF (2009) Strain localization in vesicular magma: implications for rheology and fragmentation. Geology 37(11):1023–1026. https://doi.org/10.1130/G30199A.1

Zandomeneghi D, Voltolini M, Mancini L, Brun F, Dreossi D, Polacci M (2010) Quantitative analysis of X-ray microtomography images of geomaterials: application to volcanic rocks. Geosphere 6:793–804

Zhang Y (1999) A criterion for the fragmentation of bubbly magma based on brittle failure theory. Nature 402:648–650. https://doi.org/10.1038/45210